Petrogenesis of Proterozoic Lamprophyres from the Western Dharwar Craton, southern India

A Thesis

submitted to

Indian Institute of Science Education and Research Pune in partial fulfilment of the requirements for the BS-MS Dual Degree Programme

by

Devesh Verma

IISER PUNE

Indian Institute of Science Education and Research - Pune

Dr Homi Bhabha Road,

Pashan, Pune - 411008, INDIA.

April, 2020
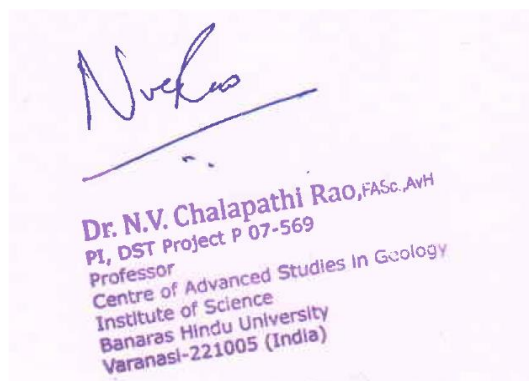Supervisor: Dr N V Chalapathi Rao
Devesh Verma

Certificate

This is to certify that this dissertation entitled "Petrogenesis of Proterozoic Lamprophyres from the Western Dharwar Craton, southern India" towards the partial fulfilment of the BS-MS dual degree programme at the Indian Institute of Science Education and Research, Pune represents study/work carried out by Devesh Verma at Banaras Hindu University, Varanasi, under the supervision of Dr N V Chalapathi Rao, Professor, Department of Geology, during the academic year 2019-2020.

Dr. N.V. Chalapathi Rao,FASc.,AvH
PI, DST Project P 07-569
Professor
Centre of Advanced Studies In Geology
Institute of Science
Banaras Hindu University
Varanasi-221005 (India)

Dr N V Chalapathi Rao

Committee:

Dr N V Chalapathi Rao

Dr Shreyas Managave

Declaration

I hereby declare that the research work presented in the report entitled "Petrogenesis of Proterozoic lamprophyres from the Western Dharwar Craton, southern India" has been carried out by me at the Department of Geology, Banaras Hindu University, under the supervision of Dr N V Chalapathi Rao and the same has not been submitted elsewhere for any other degree.

Devesh Verma

Date: 8 April, 2020

Acknowledgement

Contents

List of Figures

List of Tables

Abstract

The Proterozoic Harohalli dyke swarm lies in the Dharwar craton. Some of these dykes were sampled from Mysore to investigate the sub-surface geology of the region. Lamprophyre samples were collected since they act as windows to the SCLM.

Microscopy gave characteristic lamprophyric features – panidiomorphic-porphyritic texture with amphibole and clinopyroxene as phenocrysts and feldspar as groundmass. EPMA analysis revealed the presence of two types of amphiboles – magnesiohastingsite (primary) and actinolite (secondary). Diopsidic augite was also present. The lamprophyre was identified to be Vogesite – a calc-alkaline lamprophyre.

The lamprophyres are shoshonitic and high-K in nature. Whole-rock geochemistry showed Nb-Ta-Ti negative anomaly along with Pb, K and Sr enrichment. A negative Hf-Zr anomaly and depletion of HREE was observed. However, due to U depletion, low Mg# and Ni concentration, crustal contamination appeared to be practically absent, and with the help of tectonic discrimination diagrams, a subduction zone tectonic setting has been suggested.

The petrogenesis was pinned down to low degrees of partial melting of subduction fluid-metasomatised depleted mantle followed by high degrees of fractional crystallisation, through discrimination diagrams and petrogenetic modelling. A phlogopite garnet lherzolite source was estimated, and the metasomatized mantle was simulated by mixing average global subducting sediments and depleted mantle.

1   Introduction

The Dharwar Craton is a composite of cratonic bodies that formed in peninsular India. It is composed of tonalite-trondhjemite-granodiorite (TTG) gneisses, calc-alkaline granitoids and greenstone belts. Traditionally, it has been divided into two blocks – the Eastern and the Western Dharwar Craton - which are separated by a mylonitic zone (Swami Nath and Ramakrishnan, 1981) and a distinct decrease in the thickness of crust from the Western to the Eastern Dharwar Craton (Jayananda et al., 2018).

The Western Dharwar Craton includes the Peninsular Gneissic Complex (PGC), which is Archaean in age, along with two generations of volcanic-sedimentary greenstone sequences. It spans from the Arabian Sea to the Chitradurga greenstone belt in the east.

The Eastern Dharwar Craton consists of the Dharwar batholith, banded gneisses and thin, volcanic-rich greenstone belts and sedimentary basins. It spans from the Deccan Traps and Bastar Craton in the north to Eastern Ghats Mobile Belt in the east and the Sothern Granulite Terrane in the south. The two blocks are connected through a plutonic body called the Closepet Granite.

This project is a part of a larger study focussed on investigating the sub-surface geological nature of the two Dharwar blocks. I have worked on a suite of dyke samples from the Mysore area which are a part of the Harohalli dyke swarm, which falls in the WDC. These dyke samples showed lamprophyric appearance on the field and were collected for detailed study. Being rich in both compatible and incompatible elements, lamprophyres are expected to serve as windows to the Subcontinental Lithospheric Mantle (SCLM) – the uppermost part of mantle included in the continental lithosphere.

1.1   Lamprophyres

The term 'lamprophyre' was coined by Von Gümbel in 1874 to describe large, lustrous biotite-phenocrysts-rich rock from Fichtelgebirge, Germany. The word has its etymology in the Greek words 'lampros' and 'porphyros' which translates to 'glistening porphyry', an apt choice based on the field attributes of these rocks.

They are mostly hypabyssal (appear as dykes, sills or pipes), volatile-rich, sodic to potassic and mafic to ultramafic alkaline igneous rocks confined to the continental lithosphere. Megascopically, they are mesocratic to melanocratic rocks having a characteristic 'panidiomorphic-porphyritic' texture under the microscope which entails the presence of dominantly-euhedral phenocrysts amidst fine groundmass.

Mineralogically, they consist of hydrous ferromagnesian minerals like mica or phlogopite, amphibole and non-hydrous mafic minerals such as olivine and clinopyroxene. They lack feldspar and orthopyroxene as phenocrysts. Feldspar or feldspathoids may be present, but due to the hydrous nature of the system, they are restricted to the groundmass (Rock, 1991; Le Maitre, 2002).

Based on their mineralogy, chemical composition and tectonic association, the lamprophyres have been categorised into three groups. They are:

a) **Calc-alkaline lamprophyres (CAL)** – These are characterized by biotite or hornblende phenocrysts with alkali feldspar or plagioclase in the groundmass. They do not consist of feldspathoids. CALs are associated with granitoid plutons in orogenic belts.

b) **Alkali lamprophyres (AL):** The amphibole kaersutite or zoned titanian-augite present as phenocrysts in a groundmass containing feldspars and feldspathoids are characteristic of these lamprophyres. ALs are associated with syenite-gabbro or alkali rock-carbonatite complexes in continental rift valleys and cratons.

c) **Ultramafic lamprophyres (UML):** These can be identified by the presence of phenocrysts of phlogopite, olivine and/or augite in a groundmass containing perovskite, carbonate and/or melilite. UMLs are associated with alkali ultramafic-carbonatite centres and syenites in continental rifts.

The lamprophyres are further classified based on their mineralogy following the IUGS recommendation (Le Maitre, 2002). They also recommended against using the term 'lamprophyre clan' to include lamprophyres, lamproites and kimberlites in a group of rocks commonly associated in the field and exhibiting some common characteristics.

Table 1 The IUGS mineralogical classification of lamprophyres (Le Maitre, 2002)

Light-coloured constituents		Predominant mafic minerals		
Feld	*Foid*	*Biotite > Hornblende, ± Diopsidic augite, (± Olivine)*	*Hornblende, Diopsidic augite, ±Olivine*	*Brown amphibole, Ti-augite, Olivine, Biotite*
Or > Pl		Minette	Vogesite	
Pl > Or		Kersantite	Spessartite	
Or > Pl	Feld > Foid			Sannaite
Pl > Or	Feld > Foid			Camptonite
	Glass or Foid			Monchiquite

(Or = orthoclase, Pl = plagioclase, Feld = feldspar, Foid = feldspathoid)

Based on the enrichment of LILE and HFSE, and the highly fractionated chondrite-normalized REE pattern, in the lamprophyres, three explanations have been proposed for their melt generation. They are:

a) Garnet lherzolite undergoes very low degrees of partial melting (less than 1%), thereby suggesting a greater than 70 km deep melt generation event.

b) The mantle undergoes disequilibrium melting, involving an REE rich phase.

c) Partial melting happens in a metasomatized mantle, priorly depleted in incompatible elements.

Lamprophyres have been reported from various tectonic settings like rifted margins, arc and orogenic belts, and plume-generated intra-plate volcanic sites. Rock(1991) codified the tectono-magmatic association of lamprophyres in detail. Lamprophyres are also associated with a variety of rock suites like calc-alkaline granitoid plutons, shoshonites, alkaline syenites gabbro plutons, carbonatite-ijolite-nephelinite complexes, etc. Most of the lamprophyres have been found in the intra-plate, tectonically stable, cratonic

regimes but CAL and AL are particularly related to convergent and passive margins. UML are relatively occasional and often associate with hot spots. AL are common in rift settings.

1.2 Regional geology

Mysore district is present at the bottom of the Deccan Peninsula as the southernmost part of Karnataka State. It is located between 11°30' and 12°50'N latitudes and 75°45' and 77°45'E longitudes. The district covers an area of 11,847 km^2 (District Resource map, GSI, 1992). To the north of Mysore lie Hassan, Mandya and Bangalore districts, Cannanore district of Kerala and Udhagamandalam district of Tamil Nadu surround it from below, and Coorg district lies to the west of Mysore.

There is a major presence of granulites in the area which include charnockites, high-grade schist belts, migmatites, greenstone belts, dolerite and gabbro dykes, carbonatite, felsite and felsite porphyry (District Resource map, GSI, 1992). Mysore is the type area for the Sargur Group of rocks which are the oldest known supracrustals of Karnataka.
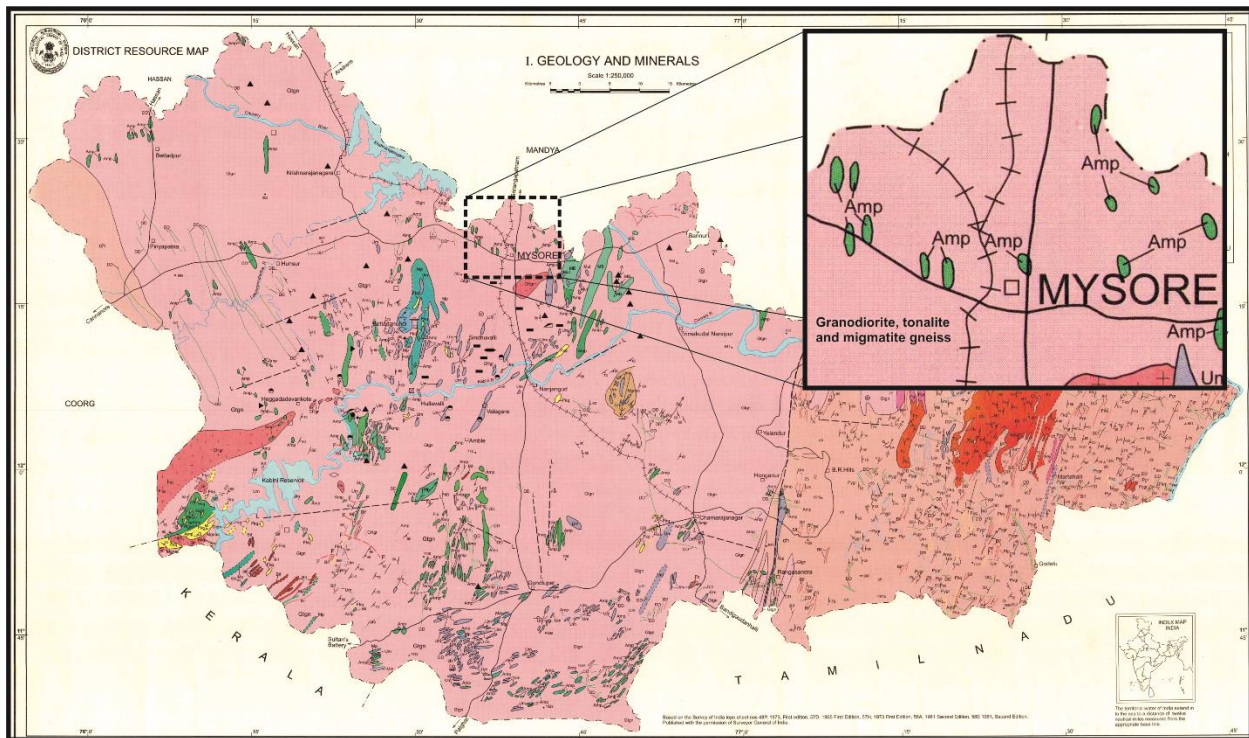
Fig 1 *District Resource map of Mysore district, Geological Survey of India (1992)*

The Peninsular Gneissic Complex (PGC) occurs as a moving terrain in central Mysore and consists of granitoids, gneisses, and migmatites which vary from granodiorite to tonalite in composition. Dharwar Supergroup greenstone belts appear as lenses in the centre of Mysore as well as its northern parts. They include meta-basalts intruded by ultramafic rocks (District Resource map, GSI, 1992).

2   Materials and Methods

Sampling

During March of 2018, Dr N V Chalapathi Rao and his students Mr D Talukdar and Ms S Raghuvanshi sampled dykes around Srirangapatnam and Belvata, Mysore and Halaguru area in Karnataka. Out of those, I have worked on 11 dyke samples collected from the Mysore area.

Thin-section preparation

Thin-sections were prepared at the in-house facility in Dept of Geology, BHU. The process of making thin sections was as follows.

Chips were obtained by chopping off the hand specimen-sized samples and washed. One flat surface of the chips was smoothened by progressive grinding using carborundum powder of increasing mesh sizes on a rotating plate at first and then on a glass plate. Next, the chips were mounted on a glass slide using a resin and hardening agent mixture and left to dry for a day. Subsequently, the mounted chips were cut off using a precision rock cutter leaving behind a fine layer of sample on the slide. This layer was then ground using carborundum powder to obtain a 30-micron thickness of the samples (ensured with the help of a microscope). Finally, the slides were polished using alumina polish on a fur mat. (Polishing is required for EPMA and SEM-EDS.)

Petrography

A detailed petrographic study of the samples was carried out, which included both megascopy and microscopy. Megascopy was carried out on the field by the sampling team, and first-order mineral identification was made.

Microscopic study was carried out using a Leica petrographic microscope and photomicrographs were taken using Leica Application Suite software. Thin sections were studied for identification of major and accessory minerals and texture of the samples.

Whole-rock chemistry

The samples were sent to Activation Laboratories, Ancaster, Canada for whole-rock chemical analysis where major and some of the trace elements were analysed using ICP-OES. Further, trace and rare-earth element (REE) concentrations were measured using multi-acid digestion and ICP-MS analysis.

Mineral chemistry

Polished thin sections were coated with a 20-nm-thin layer of carbon using LEICA-EM ACE200 instrument. Then, firstly, high-resolution BSE images were captured using Carl Zeiss Scanning Electron Microscope, EVO18 Research, and first-order point chemical analyses were carried out using EDAX EDS coupled to the SEM. Finally, 2 slides were studied using CAMECA-SXFive EPMA; point analyses and line scans were made. Both the instruments are present at the DST-SERB National Facility in the Department of Geology, BHU.

The EPMA analyses of respective minerals were grouped based on their oxide data followed by calculating cation site distribution and classification of the minerals using MS-Excel programs (that I developed) following standard classification schemes for different minerals, e.g. Leake *et al.* (1997) for amphiboles.

3   Results

3.1   Megascopy

The samples were collected off a single dyke of length ≈ 300m and width≈ 100m intruding felsic country rock. The first few samples were fine-grained shining rocks with pink coloured felsic veins. Moving further, the veins changed to aggregates of felsic material, giving the dyke a patchy appearance (fig 2b). Here, phenocryst grain size was larger than that of initial samples. Towards the end, the grain size remained almost the same, but the felsic and mafic parts roughly formed a homogeneous dyke.
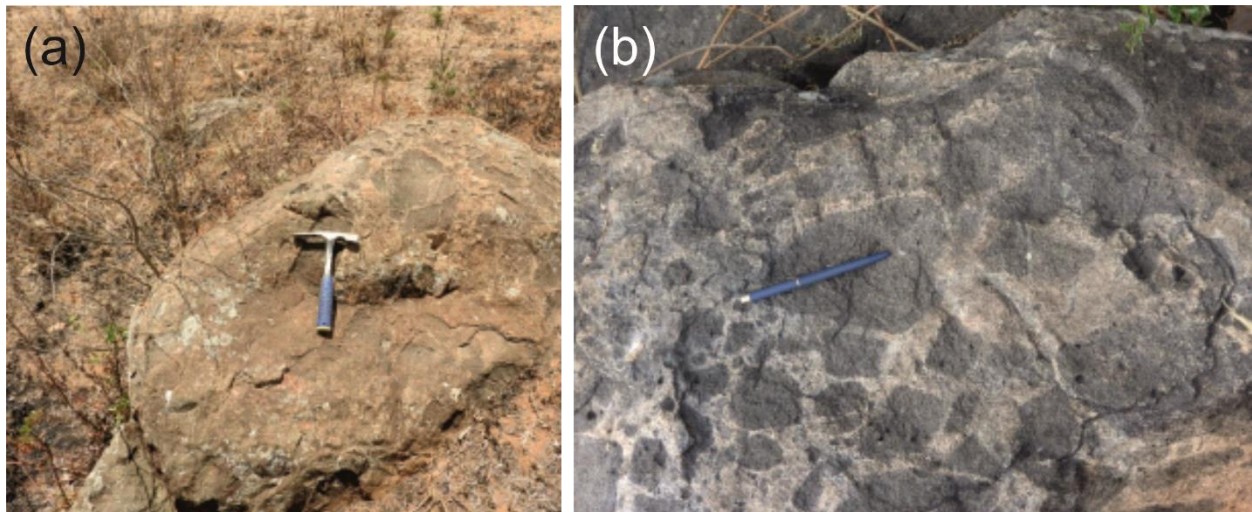
Fig 2 (a) *A boulder of the sampled dyke. **(b)** Mafic dyke showing a patchy appearance due to felsic intermingling.*

3.2   Texture

A distinct panidiomorphic-porphyritic texture (fig 3a) was observed in the samples which had euhedral to subhedral phenocrysts (acicular, prismatic and polygonal) of amphibole and clinopyroxene and feldspar restricted to fine groundmass. The groundmass showed perthite texture at some places characterised by exsolution lamellae.

The phenocrysts had multiple inclusions (fig 3c & 3d), including colourless and opaque minerals. Reaction rims were present around some of the phenocrysts, and the samples showed altered minerals (fig 3b). No xenocrysts were found in any of the samples.
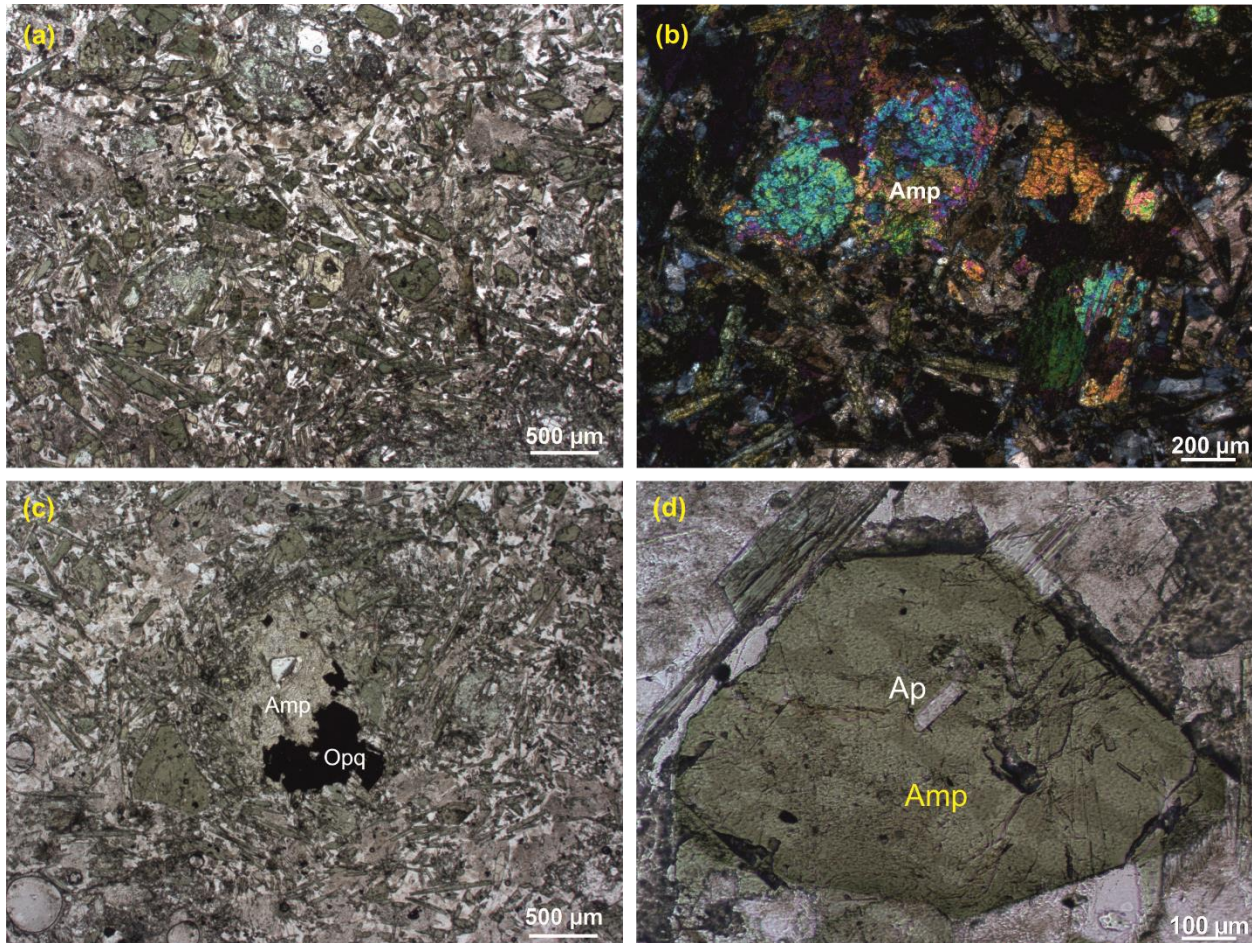
Fig 3(a) *Characteristic panidiomorphic-porphyritic texture, having amphibole and clinopyroxene phenocrysts situated in a groundmass of feldspar, PPL.* ***(b)*** *Altered amphibole grains in XPL.* ***(c)*** *An amphibole grain hosting an opaque inclusion, PPL.* ***(d)*** *An apatite inclusion in amphibole grain, PPL.*

3.3   Microscopy

The samples contained amphiboles, pyroxenes and feldspars as the major phases and chlorite, epidote, sphene (titanite), quartz, apatite and magnetite as accessory phases.

Amphibole: They were present as phenocrysts (acicular and hexagonal) and in the groundmass (acicular). Both primary (euhedral grains) and secondary amphiboles (present as reaction rims around pyroxene) (fig 5c) were found. Distinct sets of cleavage planes intersecting at 116º - 124º (fig 4c) and light to dark green pleochroism was observed. Primary amphiboles, showing extinction at 25º - 31º, were the dominant phase while secondary ones, showing extinction at 15º - 20º, were lesser in number.
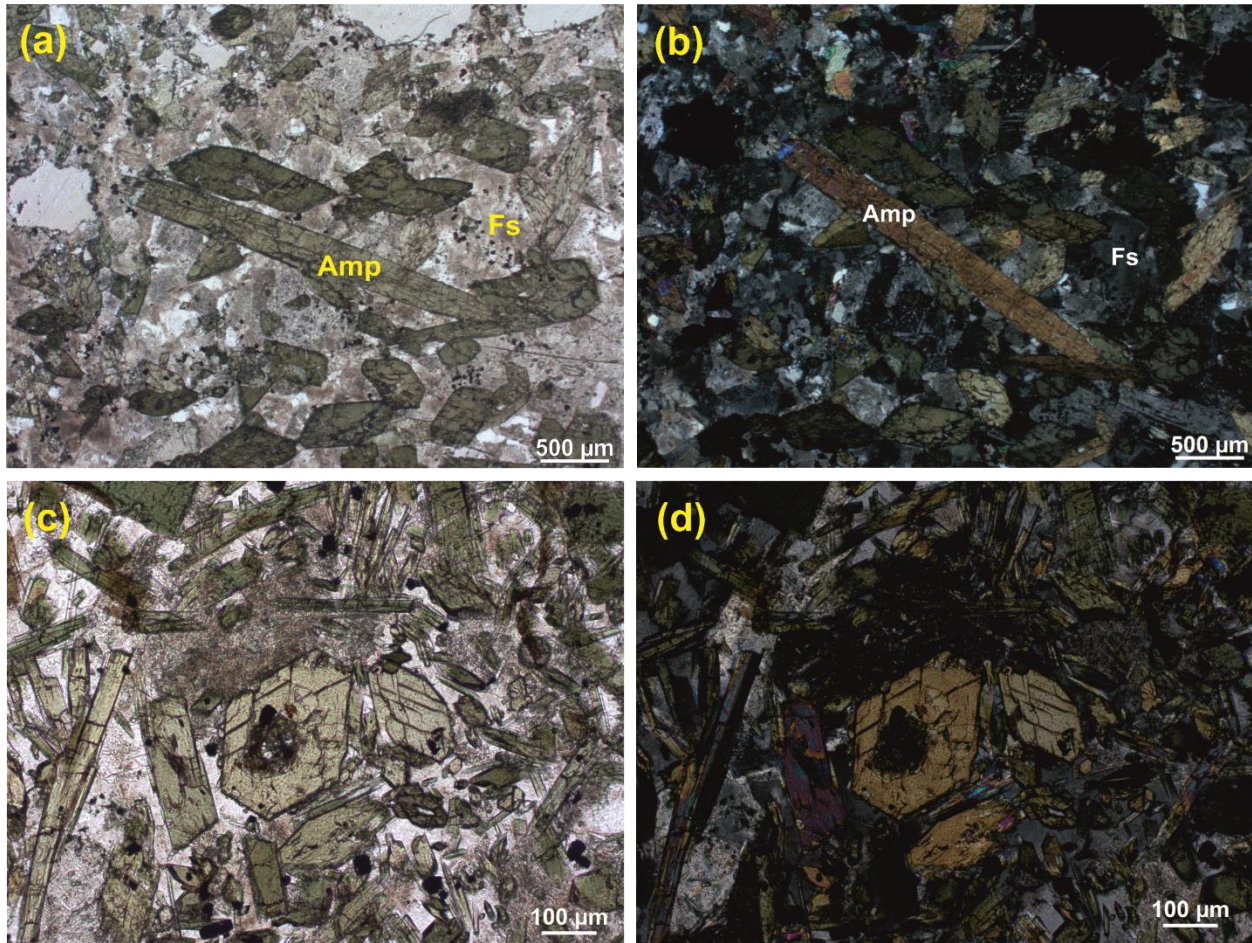
Fig 4 (a) Acicular and hexagonal amphibole grains in feldspar groundmass, PPL. *(b)* Same in XPL. *(c)* Hexagonal amphibole grains showing two distinct sets of cleavage, PPL. *(d)* Same in XPL. Second to third-order interference colours of calcic amphibole seen.

Pyroxene: They occurred as euhedral to subhedral, polygonal phenocrysts, colourless to pale brown in appearance, having cleavage planes intersecting at 86º - 95º and showing 40º - 45º extinction angle. Some of the pyroxenes were getting altered into amphiboles and showed distinct reactions rims (fig 5c and 5d).

Feldspar: They were strictly present as groundmass. Both plagioclase and alkali feldspars were present, marked by lower first-order interference colours. Lamellar twinning marked plagioclase while alkali feldspars, the more abundant species, were marked by simple twinning and Perthite texture at some places.
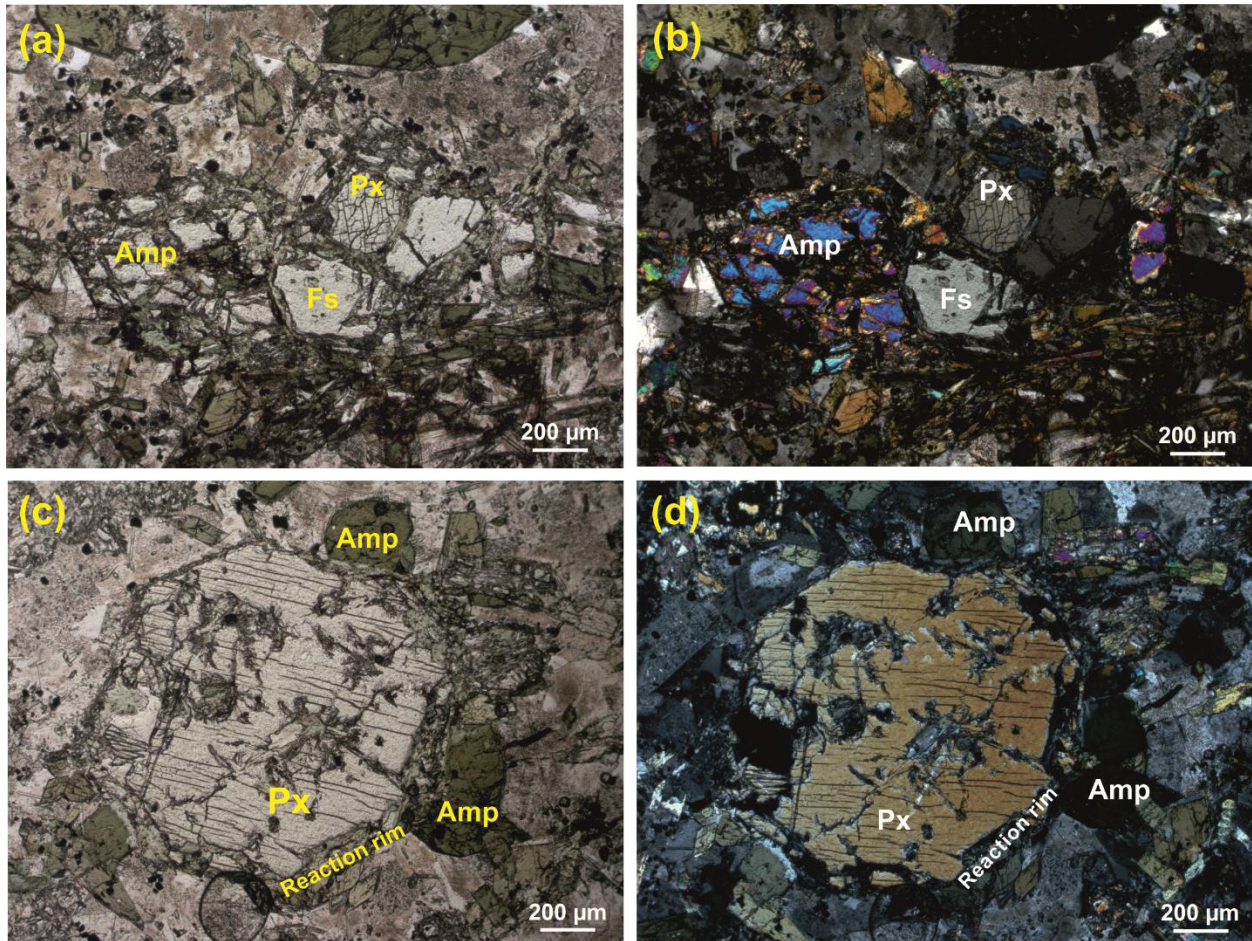
Fig 5 (a) Pyroxene grain showing fractures and cleavages, PPL. (b) Same in XPL. (c)An octahedral, altered, fractured pyroxene showing reaction rim leading to the formation of secondary amphibole, PPL. (d) Same in XPL.

Chlorite, and epidote: They were present as light and dark green, pleochroic phases, resembling amphiboles and present as products of alteration throughout the samples.

Sphene: They were dark green phases, present as inclusions in phenocrysts.

Quartz: They were colourless phases having no cleavage planes and undulose extinction.

Magnetite: They were opaque phases often present as inclusions in the phenocrysts.

Apatite: They were colourless phases often present as inclusions in the phenocrysts.

3.4   Mineral Chemistry

Amphibole

The EPMA data, upon mineral formula calculation and classification, revealed that the two types of amphiboles are both **calcic amphiboles**, i.e. $(Ca+Na)_B \geq 1.00$ and $Na_B < 0.50$, namely magnesiohastingsite and actinolite. The cation site distribution data was used to classify the amphiboles using Leake et al. (1997), and the classification plots were plotted, as shown in fig 6.

Magnesiohastingsite: It is a dark green coloured hornblende present mostly in igneous rocks as a primary amphibole. Representative analyses and cation site distribution for the same are presented in Tables 2a & 2b.

Actinolite: It is a pale to dark green coloured amphibole which showed 15º - 20º extinction angle. It was mostly present as small acicular grains. Representative analyses and cation site distribution for the same are given in Tables 3a & 3b.

The TiO_2 vs SiO_2 discrimination diagram of Rock (1991) plotted the Magnesiohastingsite mineral data in the field of primary amphiboles occurring majorly in calc-alkaline lamprophyres while actinolite mineral data fell in the field where most secondary amphiboles lie (fig 7).

Pyroxene

A large number of pyroxene grains were analysed, and the EPMA data was classified following Morimoto (1988). Wollastonite, Enstatite and Ferrosilite end-members were calculated, and it was found that the pyroxenes are Diopsidic augite (fig 8).

Feldspar

More than 50 point analyses were made on the samples, and the EPMA data was classified based on feldspar end-members. The minerals were identified as albite (Na-plagioclase), sanidine and orthoclase (K-feldspar).
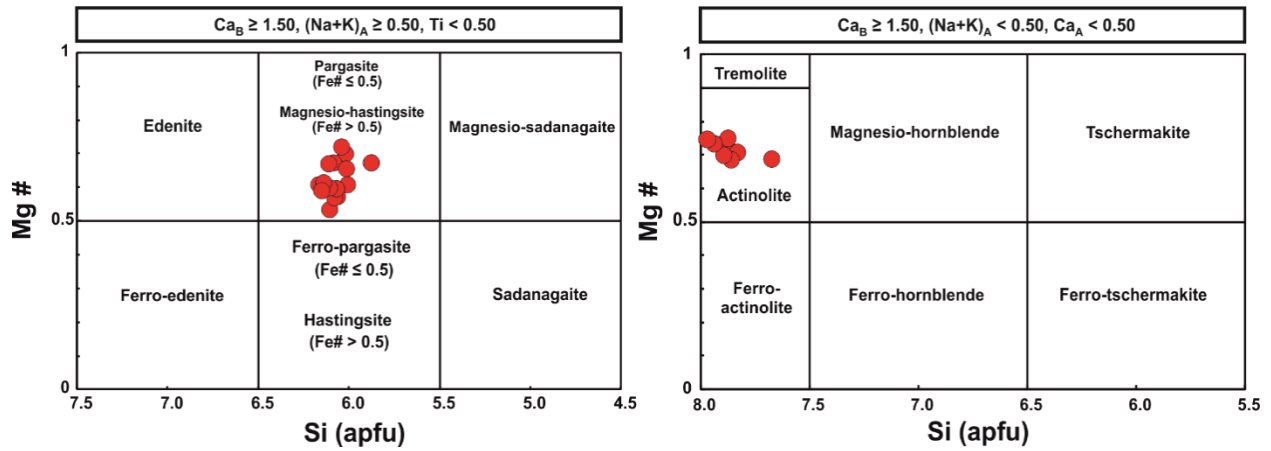
Fig 6 *Classification of amphiboles* (Leake *et al.*, 1997)
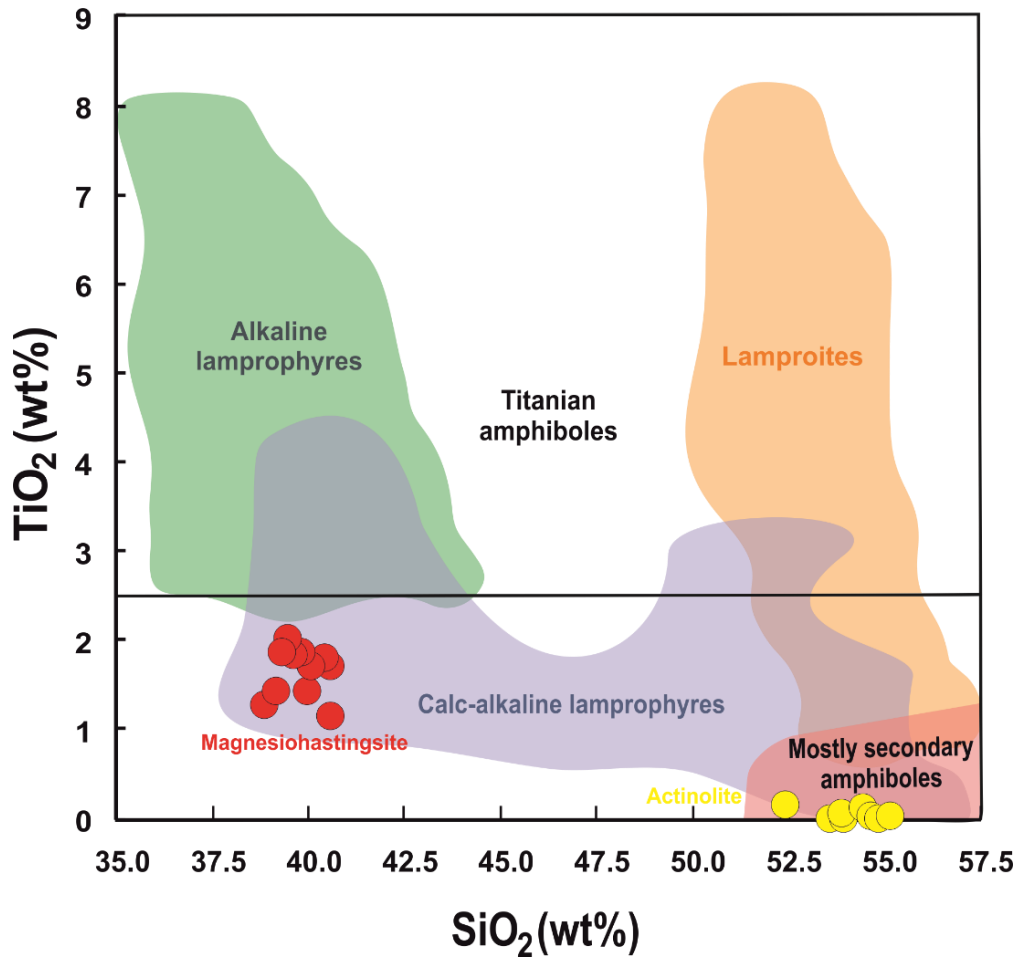
Fig 7 *Discrimination diagram for the amphiboles in lamprophyres* (Rock, 1991)

Table 2(a) Representative EPMA analyses for Magnesiohastingsite

	F	Cl	Na$_2$O	K$_2$O	MgO	CaO	MnO	FeO	Al$_2$O$_3$	Cr$_2$O$_3$	SiO$_2$	TiO$_2$	P$_2$O$_5$	Total
Mh1	0.1	0.0	2.3	1.2	12.0	11.4	0.2	14.7	12.5	0.0	40.0	1.4	0.0	**95.7**
Mh2	0.1	0.0	2.3	1.3	10.9	11.7	0.3	16.4	13.5	0.0	38.9	1.3	0.0	**96.7**
Mh3	0.2	0.1	2.1	1.2	11.0	11.7	0.4	16.1	12.8	0.1	40.1	1.7	0.1	**97.5**
Mh4	0.0	0.1	2.0	1.5	10.1	11.7	0.7	17.4	12.6	0.0	39.8	1.7	0.0	**97.7**
Mh5	0.1	0.1	1.9	1.6	9.8	11.5	0.4	16.6	12.6	0.0	39.5	2.0	0.1	**96.2**
Mh6	0.2	0.1	2.0	1.6	10.1	11.5	0.4	16.9	12.2	0.1	39.6	1.8	0.1	**96.5**
Mh7	0.3	0.1	2.0	1.6	10.5	11.3	0.4	16.3	12.0	0.1	40.6	1.7	0.1	**96.9**
Mh8	0.3	0.1	2.1	1.2	10.1	11.0	0.4	16.2	12.4	0.0	40.1	1.7	0.0	**95.5**
Mh9	0.3	0.1	2.0	1.5	10.2	11.5	0.4	15.7	12.0	0.1	39.7	1.9	0.0	**95.4**
Mh10	0.2	0.1	1.9	1.5	8.9	11.4	0.5	18.8	11.6	0.0	39.2	1.4	0.0	**95.6**
Mh11	0.2	0.0	2.2	1.4	12.2	11.8	0.2	14.0	12.6	0.1	39.9	1.8	0.1	**96.4**
Mh12	0.3	0.1	2.0	1.4	11.4	11.4	0.4	15.0	12.2	0.1	40.5	1.8	0.0	**96.5**
Mh13	0.0	0.1	2.2	1.1	10.8	11.2	0.4	15.8	13.2	0.1	40.6	1.1	0.0	**96.6**
Mh14	0.1	0.1	2.0	1.6	9.7	11.4	0.4	16.2	12.7	0.1	39.3	1.9	0.0	**95.5**
Mh15	0.0	0.1	2.0	1.5	10.1	11.2	0.2	16.6	12.2	0.1	39.8	1.8	0.0	**95.7**

Values in weight %

Table 2(b) Cation site distribution for Magnesiohastingsite

	Si	Al	Ti	Cr	Fe^{3+}	Fe^{2+}	Mg	Mn	Ca	Na	K
Mh1	6.0	2.2	0.2	0.0	0.8	1.0	2.7	0.0	1.8	0.7	0.2
Mh2	5.9	2.4	0.1	0.0	0.9	1.2	2.5	0.0	1.9	0.7	0.2
Mh3	6.0	2.3	0.2	0.0	0.7	1.3	2.5	0.0	1.9	0.6	0.2
Mh4	6.0	2.2	0.2	0.0	0.7	1.5	2.3	0.1	1.9	0.6	0.3
Mh5	6.1	2.3	0.2	0.0	0.4	1.7	2.2	0.1	1.9	0.6	0.3
Mh6	6.1	2.2	0.2	0.0	0.6	1.6	2.3	0.1	1.9	0.6	0.3
Mh7	6.2	2.1	0.2	0.0	0.5	1.5	2.4	0.0	1.8	0.6	0.3
Mh8	6.1	2.2	0.2	0.0	0.6	1.5	2.3	0.0	1.8	0.6	0.2
Mh9	6.1	2.2	0.2	0.0	0.4	1.7	2.4	0.0	1.9	0.6	0.3
Mh10	6.1	2.1	0.2	0.0	0.6	1.8	2.1	0.1	1.9	0.6	0.3
Mh11	6.0	2.2	0.2	0.0	0.6	1.2	2.7	0.0	1.9	0.7	0.3
Mh12	6.1	2.2	0.2	0.0	0.6	1.3	2.6	0.0	1.9	0.6	0.3
Mh13	6.1	2.3	0.1	0.0	0.8	1.2	2.4	0.1	1.8	0.6	0.2
Mh14	6.1	2.3	0.2	0.0	0.4	1.7	2.2	0.1	1.9	0.6	0.3
Mh15	6.1	2.2	0.2	0.0	0.6	1.5	2.3	0.0	1.8	0.6	0.3

Values in a.p.f.u. (calculated for 23 oxygen atoms, rounded off to 1 decimal place)

Table 3(a) Representative EPMA analyses for Actinolite

	F	Cl	Na$_2$O	K$_2$O	MgO	CaO	MnO	FeO	Al$_2$O$_3$	Cr$_2$O$_3$	SiO$_2$	TiO$_2$	P$_2$O$_5$	Total
Ac1	0.0	0.0	0.2	0.1	16.1	12.3	0.4	11.5	0.9	0.2	54.7	0.0	0.0	**96.5**
Ac2	0.1	0.0	0.2	0.1	15.6	12.4	0.4	12.9	0.9	0.2	54.8	0.0	0.1	**97.7**
Ac3	0.0	0.0	0.2	0.1	16.6	12.4	0.4	10.6	0.5	0.1	54.9	0.0	0.0	**95.8**
Ac4	0.0	0.0	0.2	0.1	14.8	12.3	0.4	13.5	1.2	0.1	53.6	0.0	0.0	**96.2**
Ac5	0.1	0.0	0.6	0.2	13.8	11.5	0.8	15.3	1.8	0.1	52.4	0.1	0.1	**96.9**
Ac6	0.2	0.0	0.5	0.1	15.0	11.8	0.5	13.9	0.9	0.2	53.9	0.1	0.0	**97.1**
Ac7	0.0	0.0	0.4	0.1	15.9	11.8	0.2	11.9	0.6	0.1	54.5	0.1	0.0	**95.7**
Ac8	0.0	0.0	0.2	0.1	15.7	12.6	0.4	11.9	1.0	0.5	54.0	0.0	0.0	**96.5**
Ac9	0.0	0.0	0.3	0.1	16.6	12.3	0.2	11.3	1.1	0.4	55.2	0.0	0.1	**97.7**

Values in weight %

Table 3(b) Cation site distribution for Actinolite

	Si	Al	Ti	Cr	Fe^{3+}	Fe^{2+}	Mg	Mn	Ca	Na	K
Ac1	7.9	0.2	0.0	0.0	0.1	1.3	3.5	0.0	1.9	0.1	0.0
Ac2	7.9	0.1	0.0	0.0	0.1	1.4	3.3	0.1	1.9	0.1	0.0
Ac3	8.0	0.1	0.0	0.0	0.0	1.3	3.6	0.0	1.9	0.0	0.0
Ac4	7.9	0.2	0.0	0.0	0.1	1.5	3.2	0.0	1.9	0.1	0.0
Ac5	7.7	0.3	0.0	0.0	0.5	1.4	3.0	0.1	1.8	0.2	0.0
Ac6	7.8	0.1	0.0	0.0	0.3	1.4	3.2	0.1	1.8	0.1	0.0
Ac7	7.9	0.1	0.0	0.0	0.2	1.3	3.5	0.0	1.8	0.1	0.0
Ac8	7.9	0.2	0.0	0.1	0.0	1.4	3.4	0.0	2.0	0.1	0.0
Ac9	7.9	0.2	0.0	0.0	0.2	1.2	3.5	0.0	1.9	0.1	0.0

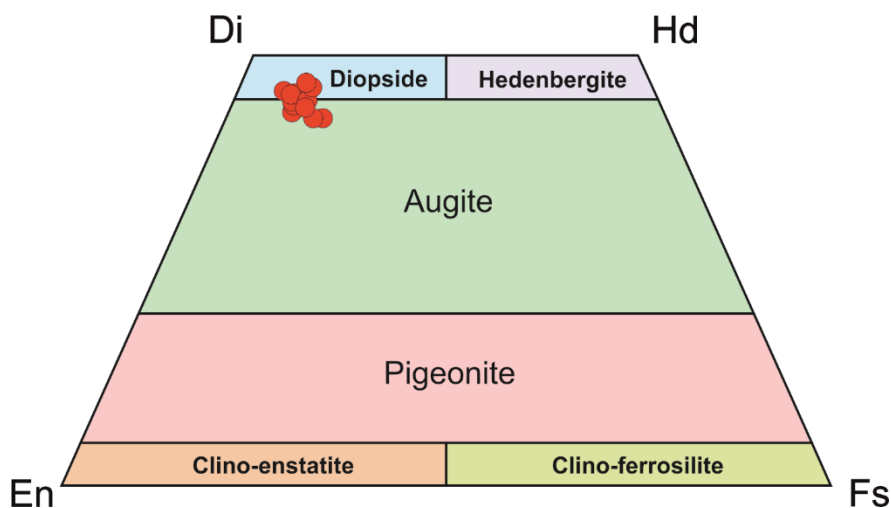Values in a.p.f.u. (calculated for 23 oxygen atoms, rounded off to 1 decimal place)

Fig 8 *The pyroxene quadrilateral used for classification of pyroxene data* (Morimoto, 1988)*.*

Table 4(a) Representative EPMA analyses for Diopsidic augite

	F	Cl	Na$_2$O	K$_2$O	MgO	CaO	MnO	FeO	Al$_2$O$_3$	Cr$_2$O$_3$	SiO$_2$	TiO$_2$	P$_2$O$_5$	Total
Px1	0.0	0.0	0.3	0.0	17.2	23.0	0.1	4.5	1.5	0.6	52.7	0.2	0.1	**100.1**
Px2	0.1	0.0	0.4	0.0	16.3	22.3	0.3	5.9	1.7	0.6	52.2	0.2	0.1	**100.0**
Px3	0.0	0.0	0.4	0.0	17.1	22.0	0.1	5.0	1.7	0.9	52.7	0.2	0.0	**100.2**
Px4	0.0	0.0	0.3	0.1	16.8	22.6	0.1	4.5	1.5	0.7	52.9	0.2	0.0	**99.8**
Px5	0.0	0.0	0.3	0.0	17.0	22.9	0.0	4.8	1.5	0.2	53.2	0.1	0.1	**100.2**
Px6	0.0	0.0	0.2	0.0	17.4	22.6	0.2	4.8	1.6	0.6	52.8	0.2	0.1	**100.6**
Px7	0.2	0.0	0.4	0.0	15.7	20.9	0.2	7.8	1.4	0.0	52.4	0.2	0.0	**99.2**
Px8	0.0	0.0	0.3	0.0	16.7	22.0	0.1	6.3	1.5	0.1	51.6	0.2	0.0	**98.9**
Px9	0.0	0.0	0.3	0.0	16.7	21.5	0.2	4.8	1.9	0.2	53.2	0.2	0.1	**99.3**
Px10	0.0	0.0	0.3	0.0	17.4	21.7	0.1	5.2	1.6	0.3	52.4	0.2	0.1	**99.2**
Px11	0.0	0.0	0.5	0.0	16.5	21.4	0.2	7.3	2.0	0.3	51.0	0.2	0.0	**99.3**
Px12	0.1	0.0	0.3	0.0	15.7	22.9	0.1	6.1	1.4	0.1	52.7	0.1	0.0	**99.5**
Px13	0.1	0.0	0.3	0.0	17.6	23.6	0.1	4.3	1.3	0.8	53.2	0.2	0.0	**101.4**
Px14	0.0	0.0	0.4	0.0	15.6	22.6	0.4	4.9	2.0	0.7	52.0	0.1	0.0	**98.6**
Px15	0.0	0.0	0.2	0.0	17.2	22.7	0.1	3.7	1.5	1.0	52.8	0.1	0.0	**99.5**

Values in weight %

Table 4(b) Cation site distribution for Diopsidic augite

	Si	Al	Ti	Cr	Fe^{3+}	Fe^{2+}	Mg	Mn	Ca	Na	K
Px1	1.9	0.1	0.0	0.0	0.1	0.0	0.9	0.0	0.9	0.0	0.0
Px2	1.9	0.1	0.0	0.0	0.1	0.1	0.9	0.0	0.9	0.0	0.0
Px3	1.9	0.1	0.0	0.0	0.1	0.1	0.9	0.0	0.9	0.0	0.0
Px4	1.9	0.1	0.0	0.0	0.1	0.1	0.9	0.0	0.9	0.0	0.0
Px5	2.0	0.1	0.0	0.0	0.1	0.1	0.9	0.0	0.9	0.0	0.0
Px6	1.9	0.1	0.0	0.0	0.1	0.1	0.9	0.0	0.9	0.0	0.0
Px7	2.0	0.1	0.0	0.0	0.1	0.2	0.9	0.0	0.8	0.0	0.0
Px8	1.9	0.1	0.0	0.0	0.1	0.1	0.9	0.0	0.9	0.0	0.0
Px9	2.0	0.1	0.0	0.0	0.0	0.1	0.9	0.0	0.8	0.0	0.0
Px10	1.9	0.1	0.0	0.0	0.1	0.1	1.0	0.0	0.9	0.0	0.0
Px11	1.9	0.1	0.0	0.0	0.2	0.1	0.9	0.0	0.9	0.0	0.0
Px12	2.0	0.1	0.0	0.0	0.1	0.1	0.9	0.0	0.9	0.0	0.0
Px13	1.9	0.1	0.0	0.0	0.1	0.0	1.0	0.0	0.9	0.0	0.0
Px14	1.9	0.1	0.0	0.0	0.0	0.1	0.9	0.0	0.9	0.0	0.0
Px15	1.9	0.1	0.0	0.0	0.0	0.1	0.9	0.0	0.9	0.0	0.0

Values in a.p.f.u. (calculated for 6 oxygen atoms, rounded off to 1 decimal place)

Table 5(a) Representative EPMA analyses for Feldspar

	F	Cl	Na₂O	K₂O	MgO	CaO	MnO	FeO	Al₂O₃	Cr₂O₃	SiO₂	TiO₂	P₂O₅	Total
Fls1	0.2	0.0	5.7	12.6	0.0	0.0	0.0	0.1	18.4	0.0	64.6	0.0	0.0	**101.7**
Fls2	0.0	0.0	0.3	16.6	0.0	0.0	0.0	0.2	17.8	0.0	64.5	0.0	0.0	**99.4**
Fls3	0.1	0.0	0.3	16.7	0.0	0.0	0.0	0.4	18.1	0.0	63.7	0.0	0.0	**99.3**
Fls4	0.0	0.0	0.2	17.3	0.0	0.1	0.0	0.0	18.4	0.0	63.8	0.0	0.0	**99.7**
Fls5	0.1	0.0	11.9	0.0	0.0	0.2	0.0	0.0	19.3	0.0	67.8	0.0	0.0	**99.4**
Fls6	0.2	0.0	12.0	0.0	0.0	0.1	0.0	0.1	19.5	0.0	67.7	0.0	0.0	**99.6**
Fls7	0.0	0.0	7.1	6.1	0.0	0.1	0.0	0.2	18.4	0.0	66.1	0.0	0.0	**98.0**
Fls8	0.0	0.0	0.2	17.1	0.0	0.0	0.1	0.0	18.2	0.2	63.4	0.0	0.1	**99.2**
Fls9	0.2	0.0	0.1	17.2	0.0	0.0	0.0	0.1	18.1	0.1	64.2	0.0	0.0	**100.1**
Fls10	0.0	0.0	0.5	16.4	0.0	0.0	0.0	0.2	18.3	0.1	64.0	0.0	0.1	**99.6**
Fls11	0.0	0.0	12.4	0.0	0.0	0.0	0.0	0.3	19.6	0.1	68.7	0.0	0.0	**101.1**
Fls12	0.0	0.0	11.6	0.1	0.0	0.2	0.0	0.2	19.5	0.2	68.0	0.0	0.0	**99.8**
Fls13	0.0	0.0	11.7	0.1	0.0	0.4	0.1	0.1	19.8	0.1	67.5	0.0	0.1	**100.0**
Fls14	0.0	0.0	11.1	0.2	0.0	0.4	0.1	0.0	20.0	0.2	67.4	0.0	0.1	**99.5**
Fls15	0.0	0.0	11.0	0.2	0.0	0.9	0.1	0.3	20.3	0.2	66.6	0.0	0.0	**99.6**

Values in weight %

Table 5(b) Cation site distribution for Feldspar

	Si	Al	Ti	Cr	Mg	Fe²⁺	Mn	Ca	Na	K
Fs1	2.9	1.0	0.0	0.0	0.0	0.0	0.0	0.0	0.5	0.7
Fs2	3.0	1.0	0.0	0.0	0.0	0.0	0.0	0.0	0.0	1.0
Fs3	3.0	1.0	0.0	0.0	0.0	0.0	0.0	0.0	0.0	1.0
Fs4	3.0	1.0	0.0	0.0	0.0	0.0	0.0	0.0	0.0	1.0
Fs5	3.0	1.0	0.0	0.0	0.0	0.0	0.0	0.0	1.0	0.0
Fs6	3.0	1.0	0.0	0.0	0.0	0.0	0.0	0.0	1.0	0.0
Fs7	3.0	1.0	0.0	0.0	0.0	0.0	0.0	0.0	0.6	0.4
Fs8	3.0	1.0	0.0	0.0	0.0	0.0	0.0	0.0	0.0	1.0
Fs9	3.0	1.0	0.0	0.0	0.0	0.0	0.0	0.0	0.0	1.0
Fs10	3.0	1.0	0.0	0.0	0.0	0.0	0.0	0.0	0.0	1.0
Fs11	3.0	1.0	0.0	0.0	0.0	0.0	0.0	0.0	1.0	0.0
Fs12	3.0	1.0	0.0	0.0	0.0	0.0	0.0	0.0	1.0	0.0
Fs13	3.0	1.0	0.0	0.0	0.0	0.0	0.0	0.0	1.0	0.0
Fs14	3.0	1.0	0.0	0.0	0.0	0.0	0.0	0.0	0.9	0.0
Fs15	2.9	1.1	0.0	0.0	0.0	0.0	0.0	0.0	0.9	0.0

Values in a.p.f.u. (calculated for 32 oxygen atoms, rounded off to 1 decimal place)
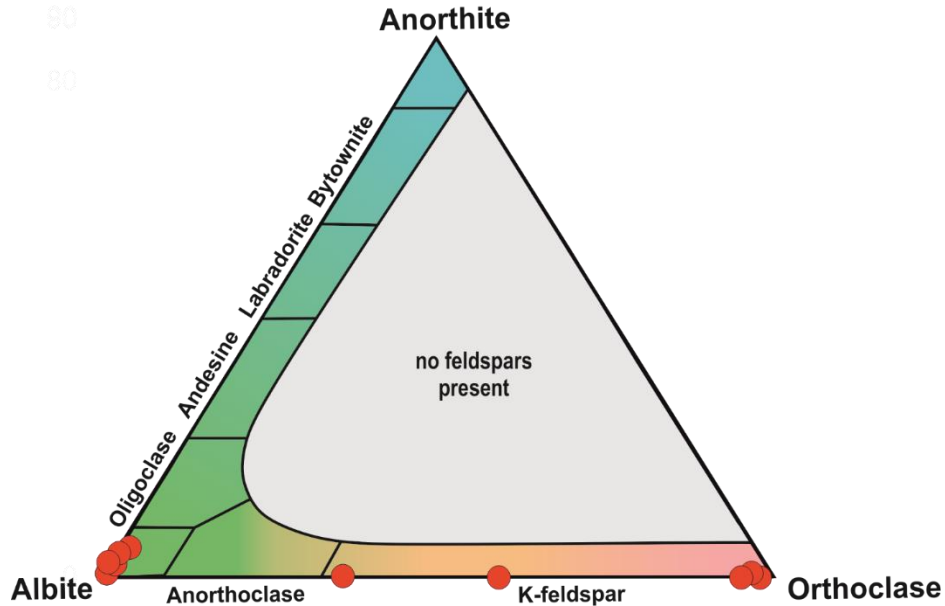
Fig 9 *Classification of feldspars.*

3.5 Whole-rock chemistry

The whole-rock major oxide and trace element data is given here.

Table 6 Whole-rock major oxide data

	SRMY 1	SRMY 5	SRMY 5.2	SRMY 5.3	SRMY 7.2	SRMY 8.3	SRMY 9	SRMY 9.2	SRMY 9.3	SRMY 10.1	SRMY 10.2
SiO_2	54.3	50.6	50.4	51.7	50.1	49.2	49.7	49.2	47.8	49.5	50.1
Al_2O_3	15.0	13.4	13.2	13.8	11.0	11.5	11.5	11.8	11.5	13.9	13.1
Fe_2O_3	9.0	11.1	12.0	11.1	11.6	11.9	11.7	11.5	13.0	12.5	12.2
MgO	4.2	6.4	6.6	5.4	8.8	8.7	8.1	7.6	8.6	6.1	6.6
CaO	7.1	8.1	7.9	8.7	10.3	9.5	9.9	9.7	8.1	8.0	8.2
Na_2O	3.5	2.9	2.8	2.7	2.3	2.2	2.5	2.4	2.2	2.9	2.8
K_2O	3.9	3.4	3.1	3.2	2.6	2.6	2.5	3.1	2.1	3.1	3.2
TiO_2	0.6	0.8	0.9	0.8	0.8	0.9	0.8	0.8	1.0	0.9	0.9
P_2O_5	0.5	0.6	0.7	0.6	0.7	0.7	0.7	0.7	0.9	0.8	0.7
MnO	0.2	0.2	0.2	0.2	0.2	0.2	0.2	0.2	0.2	0.2	0.2
Cr_2O_3	0.0	0.0	0.1	0.0	0.1	0.1	0.1	0.1	0.1	0.0	0.0
LOI	1.3	1.9	1.8	1.3	1.2	2.1	1.9	2.3	4.2	1.6	1.5
Total	**99.6**	**99.6**	**99.6**	**99.6**	**99.6**	**99.6**	**99.7**	**99.6**	**99.6**	**99.6**	**99.7**

Values in weight %

Table 6 Whole-rock trace element data

	SRMY 1	SRMY 5	SRMY 5.2	SRMY 5.3	SRMY 7.2	SRMY 8.3	SRMY 9	SRMY 9.2	SRMY 9.3	SRMY 10.1	SRMY 10.2
Ba	966	1079	923	837	795	798	727	1108	609	917	982
Ni	46	62	76	42	148	128	118	106	111	45	48
Sc	19	27	30	25	33	33	31	30	31	27	29
Be	3.0	4.0	4.0	-	-	2.0	3.0	-	1.0	4.0	4.0
Co	24.7	34.1	41.8	28.2	48.0	48.1	44.2	44.1	50.8	41.4	40.6
Cs	0.8	0.8	0.6	0.5	0.4	0.5	0.4	0.6	0.5	0.7	0.6
Ga	18.2	15.3	14.1	13.8	11.2	12.3	10.1	10.6	13.9	11.5	12.3
Hf	3.2	3.4	3.0	2.8	2.6	2.7	2.9	2.7	2.6	3.1	2.7
Nb	6.2	7.2	6.4	5.4	5.8	5.4	5.8	5.1	5.3	5.6	5.7
Rb	106.5	87.6	83.5	84.9	67.3	68.2	66.6	85.9	54.7	85.9	92.3
Sn	-	1.0	1.0	1.0	1.0	-	1.0	-	-	1.0	1.0
Sr	1532	1061	1144	1732	907	975	880	1001	715	1233	982
Ta	0.3	0.3	0.3	0.3	0.4	0.3	0.3	0.4	0.2	0.4	0.3
Th	10.5	8.8	8.1	9.4	7.9	7.6	8.1	8.9	7.6	8.3	8.9
U	1.7	1.4	1.7	2.0	1.7	1.3	1.6	1.6	1.9	1.4	1.8
V	168	234	255	245	247	262	253	245	280	267	256
W	-	-	-	-	-	-	0.6	0.5	-	0.5	0.7
Zr	128	124	113	118	105	102	105	102	95	109	108
Y	27.2	27.9	30.2	29.6	24.2	23.6	22.7	24.4	20.9	29.8	21.2
La	50.4	48.5	48.7	50.9	42.8	43.2	42.0	45.4	43.3	51.1	44.7
Ce	88	93	88	86	79	84	84	84	85	93	83
Pr	10.9	12.0	11.9	11.5	10.0	10.3	10.0	10.3	10.4	12.4	10.1
Nd	44.1	47.6	49.3	46.7	41.9	43.0	40.9	41.8	41.2	51.1	41.6
Sm	8.4	9.0	8.8	8.7	7.9	8.1	8.0	8.1	7.7	9.8	7.4
Eu	2.2	2.4	2.2	2.3	2.0	2.0	2.1	2.1	2.0	2.5	1.9
Gd	7.3	7.7	7.8	8.0	6.3	6.9	6.6	6.6	6.4	8.3	6.1
Tb	0.9	1.0	1.1	1.1	0.8	0.9	0.9	0.9	0.8	1.1	0.8
Dy	5.2	5.6	5.6	6.0	4.2	4.7	4.2	4.5	4.1	5.9	4.1
Ho	0.9	1.1	1.0	1.1	0.8	0.8	0.9	0.8	0.8	1.1	0.8
Er	2.5	3.1	3.0	3.2	2.3	2.3	2.3	2.4	2.0	3.0	2.2
Tm	0.4	0.4	0.4	0.5	0.3	0.3	0.3	0.3	0.3	0.4	0.3
Yb	2.3	2.8	2.6	3.1	2.0	2.0	2.0	2.1	1.9	2.5	2.0
Lu	0.4	0.4	0.4	0.5	0.3	0.3	0.3	0.3	0.3	0.4	0.3
Mo	2.4	1.3	0.6	0.7	1.5	1.3	1.9	1.8	1.2	1.1	1.5
Cu	49	49	67	54	93	69	72	94	267	97	64
Pb	11.8	6.3	6.9	9.2	10.3	11.5	8.0	11.2	3.1	11.5	10.7
Zn	28	49	64	44	41	53	43	36	71	48	59
Ni	29.9	43.3	57.5	26.1	94.3	86.4	72.5	64.6	91.7	31.6	33.3

All values are in ppm. Values below the detection limit are represented with a dash (–).

On the Total Alkali vs Silica diagram (fig 10), the samples fell on the Basalt, Trachy-basalt, Basaltic-trachy-andesite fields and classified, in general, as alkaline rocks.
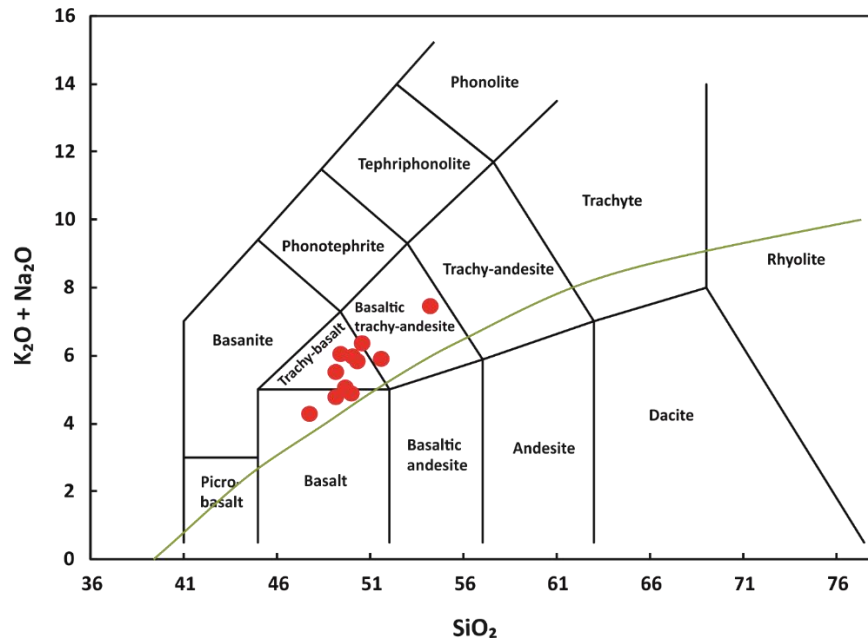

Fig 10 *Total alkali vs Silica diagram for volcanic rocks* (Le Maitre, 2002)*. The green curve divides the diagram into alkaline (upper) and sub-alkaline (lower) regions (Irvine and Baragar, 1971).*

Binary diagrams (fig 11) showed a good negative correlation of MgO with SiO_2, Al_2O_3, Na_2O and K_2O while a positive correlation was seen with CaO and P_2O_5. The negative correlation between MgO and SiO_2 implies the evolution of magma from mafic to felsic.
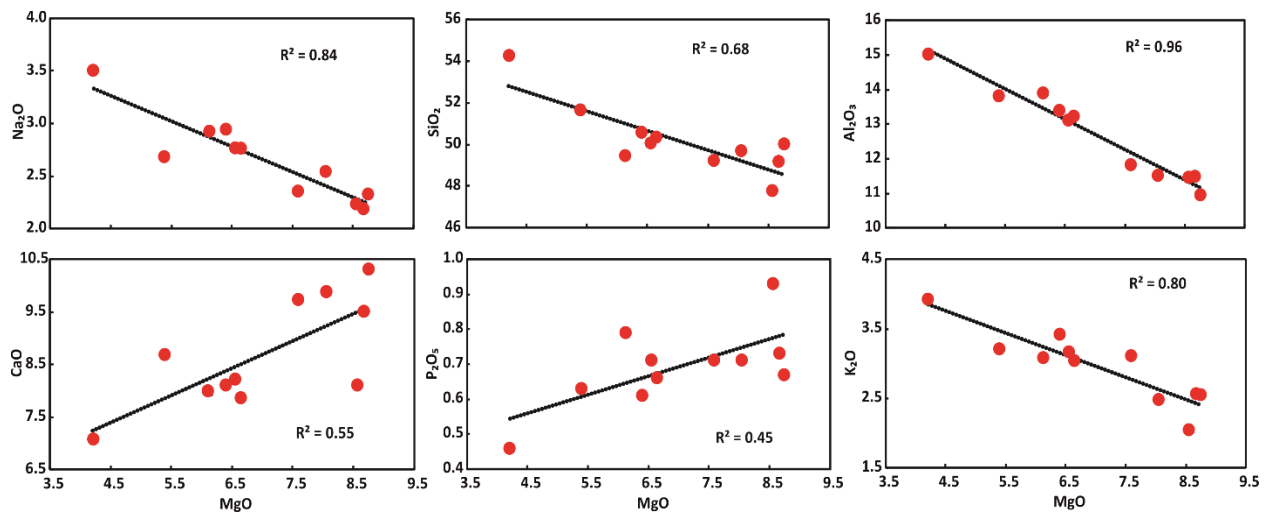
Fig 11 *Binary diagrams between MgO and other major oxides*

19

The MgO vs SiO$_2$ and Al$_2$O$_3$ vs TiO$_2$ discrimination diagrams were plotted and the samples fell in the overlap between the fields of CAL and Superior Province Shoshonitic Lamprophyres (fig 12a & 12b).
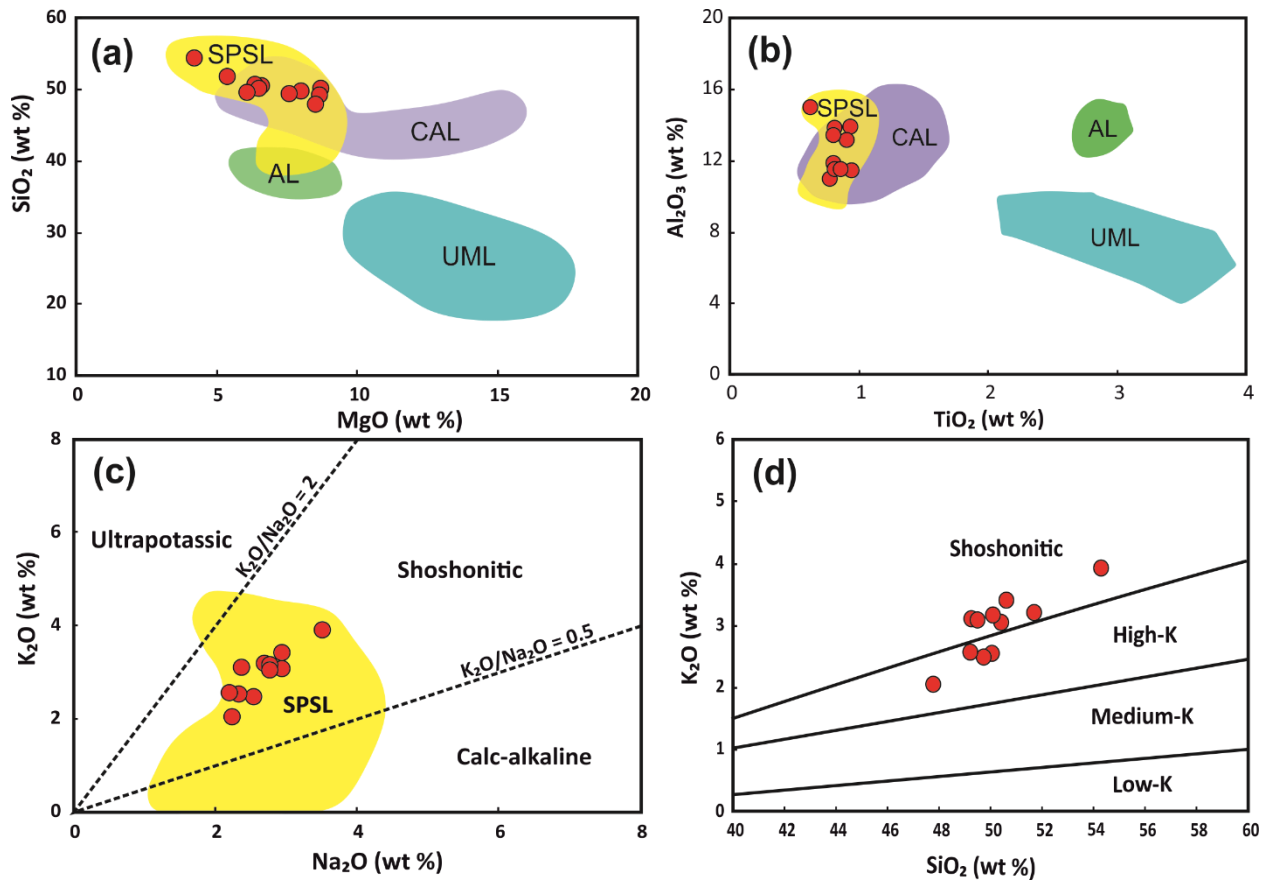
Fig 12 (a) *SiO$_2$ vs MgO and **(b)** Al$_2$O$_3$ vs TiO$_2$ discrimination diagrams for lamprophyres (Lefebvre et al., 2005). **(c)** K$_2$O vs Na$_2$O diagram (Turner et al., 1996) and **(d)** K$_2$O vs SiO$_2$ diagram (Peccerillo and Turner, 1976) for geochemical characterisation of the samples. SPSL = Superior Province Shoshonitic Lamprophyres, Canada (data from Wyman and Kerrich, 1989).*

Further, plotting the samples on the K$_2$O vs Na$_2$O classification diagram (fig 12c) reinforced the shoshonitic nature of these rocks while the K2O vs SiO2 diagram (fig 12d) classified these rocks as high-K and shoshonitic.

The chondrite-normalised REE concentrations of the samples were plotted on a spidergram (fig 13). The samples showed high fractionation between the LREE and HREE, having average (La/Lu)$_N$ = 14.5, and lower fractionation between the MREE and
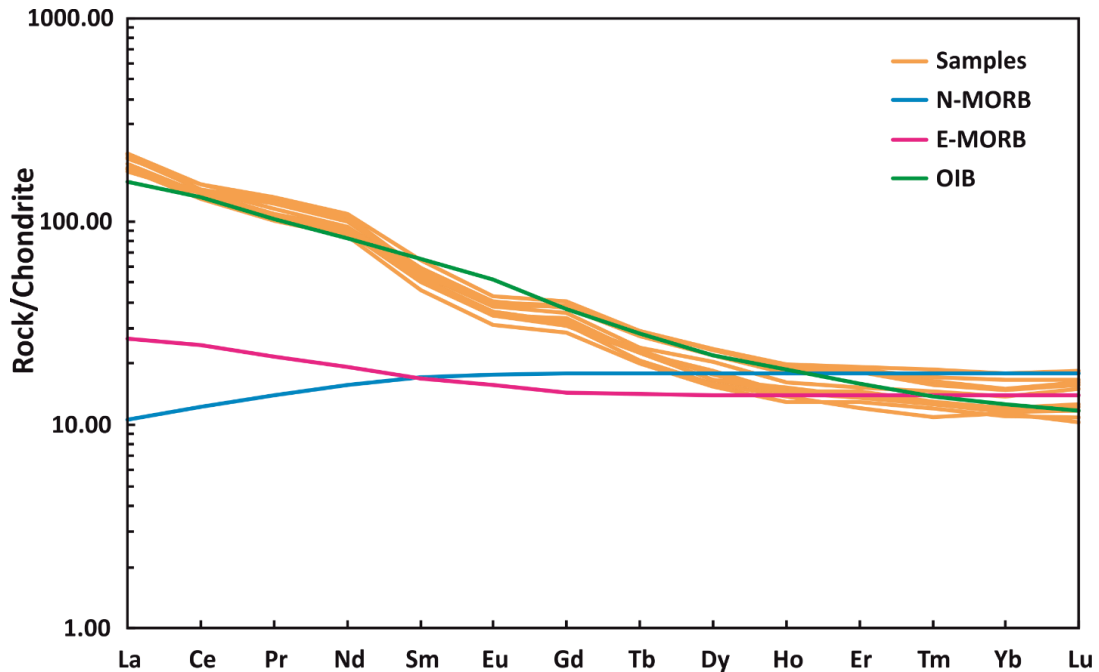
Fig 13 *REE spidergram of the samples with chondrite-normalised concentrations. Normalisation was done using values from* Sun and McDonough (1989)*. N-MORB = Normal Mid-Oceanic Ridge Basalt, E-MORB = Enriched Mid-Oceanic Ridge Basalt, OIB = Ocean Island Basalt.*
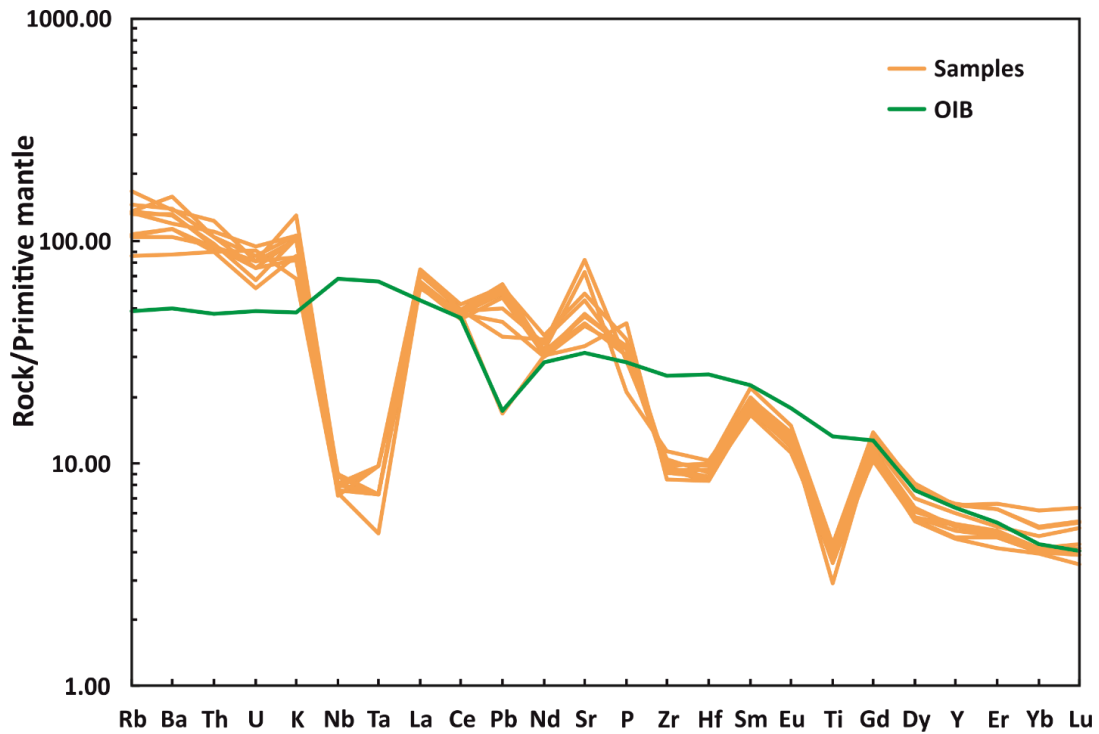

Fig 14 *Plot of Primitive mantle-normalised incompatible element concentrations. A clear T-N-T negative anomaly is visible accompanied by Zr-Hf negative anomaly and K, Pb and Sr enrichment. Normalisation was done using values from* Sun and McDonough (1989)*.*

HREE was observed with average (Gd/Lu)$_N$ = 2.5. A weak Eu anomaly $\left(\dfrac{Eu_N}{\sqrt{Sm_N \cdot Gd_N}}\right)$ was also observed, which was calculated to be equal to 0.86. The samples showed little spread and followed the REE signature of Ocean Island Basalts closely.

The primitive-mantle-normalised concentration of incompatible elements was plotted (the compatibility of the elements increasing from left to right) on a multi-element diagram (fig 14). The plot revealed a distinct negative anomaly for the elements Nb, Ta and Ti.

An enrichment of K, Pb and Sr was also observed in the samples on the plot. U showed depletion, and high LILE/REE and LILE/HFSE ratios were observed. Another distinguishing feature was the presence of a Hf-Zr negative anomaly in the samples. The overall trend of these samples roughly followed that of OIB.

4 Discussion

4.1 Classification of the samples

The collected dyke samples, for their field appearance, texture, and mineralogy, must be categorised as lamprophyres. The cognate mineralogy consisting of a hornblende, diopsidic augite, and feldspar (with plagioclase < orthoclase) further implies that these lamprophyres are Vogesites (a variety of calc-alkaline lamprophyres) in particular (Rock, 1991).

Deuteric alteration of pyroxene crystals is expected to form actinolite grains that are present as reaction rims. Hydrothermal alteration/ metasomatism of feldspar produces epidote while chloritisation of pyroxene and amphibole has occurred as well.

The presence of amphibole and pyroxene as euhedral phenocrysts suggests their early crystallisation at low cooling rates while feldspar, restricted to groundmass, must have crystallised fast but last. The apatite crystals must have also formed early since some of them are present as inclusions.

Low SiO_2, Al_2O_3, Na_2O and K_2O values for high values of MgO and vice-versa in the Harker diagrams also implies the separate crystallisation of amphibole/pyroxene and feldspar. The positive correlation of MgO with CaO and P_2O_5 can be attributed to the crystallisation of apatite, which exhausted the phosphorus oxide present in the magma.

4.2 Crustal contamination and Tectonic setting

It is essential to consider the role of crustal contamination in order to understand the petrogenesis of these rocks. No crustal xenoliths have been found in megascopic or petrographic studies. The samples show low MgO content (avg Mg# = 43.3) along with low concentrations of Ni (avg conc = 84.5 ppm) and intermediate concentrations of Cr (avg conc = 370 ppm) which suggests that either they are evolved, or there is a crustal contribution to these rocks.

Nb–Ta–Ti depletion usually implies crustal contamination or subduction zone setting since these elements are present in low concentration in the crust. The enrichment of K,

Pb and Sr in the samples suggests the same since LILE are easily transported along with fluids and also, Pb is abundantly present in the subducting sediments. However, there is an identifiable depletion of U (avg conc = 1.6 ppm) and low concentrations of Th (avg conc = 8.6 ppm) along with high MREE/HREE ratios (e.g. avg Er/Lu = 6.6 to 7.7) in these samples which question a clear role of crustal contamination.

To investigate the contribution of crustal contamination further, the Nb anomalies $\left(\frac{Nb_N}{\sqrt{Th_N \cdot Ce_N}} \right)$ and Ti anomalies $\left(\frac{Ti_N}{\sqrt{Eu_N \cdot Gd_N}} \right)$ were plotted against SiO_2 and Pb (fig 15) which act as indices of crustal contamination because of their high concentrations in the crust. The Ti anomalies showed a recognisable but insignificant negative correlation with SiO_2 while the Nb anomalies showed no correlation at all with SiO_2 or Pb. This leads us to conclude that crustal contamination does not play a significant or even a distinct role in the petrogenesis of these lamprophyres.
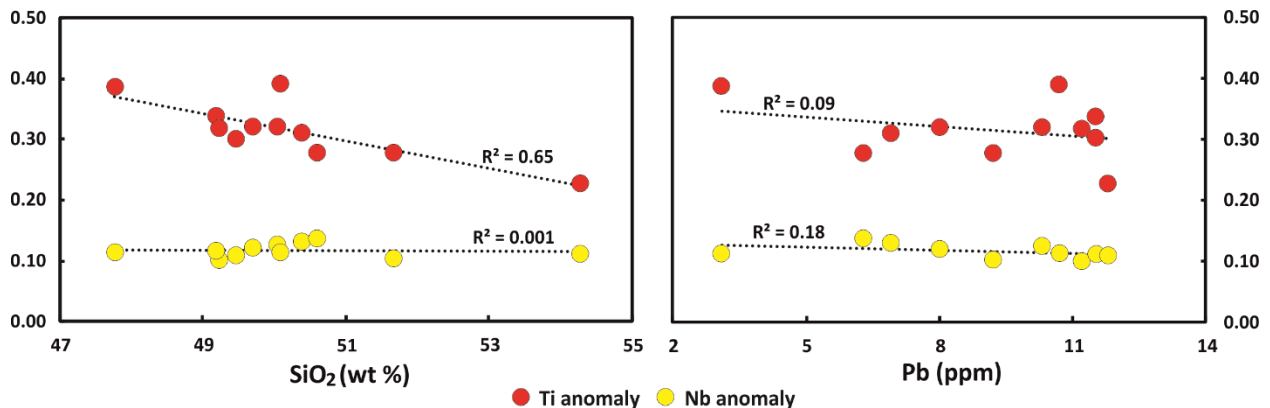

Fig 15 *Variations of Nb and Ti anomaly with SiO₂ and Pb concentration.*

Moving further, we find that even though the REE spidergram hints otherwise, the incompatible elements plot shows clear deviations from OIB signature, hence, a contribution of plume magmatism in the petrogenesis of these rocks is deemed unlikely.

This leaves us with subduction zone magmatism as the possible candidate for the petrogenesis of these rocks. In this motion, first, the TiO_2 vs K_2O discrimination diagram (Thorpe, 1987) was used. The samples fell in the field of subduction-related setting (fig 16a) in contrast to the intra-plate setting. On the Th/Yb vs Nb/Yb discrimination plot
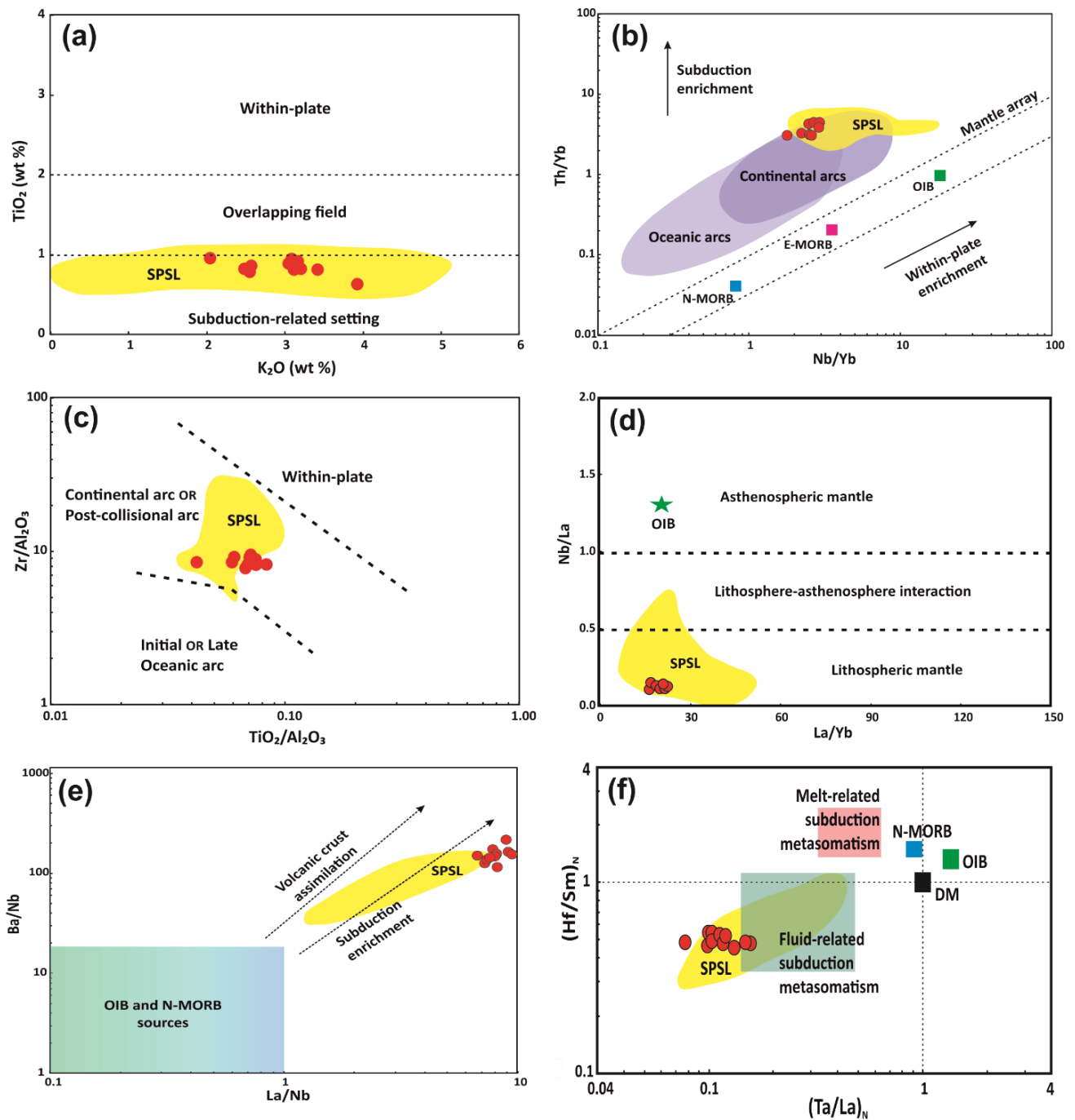
Fig 16 (a) *TiO$_2$ vs K$_2$O diagram of (Thorpe, 1987), **(b)** Th/Yb vs Nb/Yb diagram (Pearce and Peate, 1995) and **(c)** Zr/Al$_2$O$_3$ vs TiO$_2$/Al$_2$O$_3$ diagram (Muller and Groves, 2000) assign continental-arc character to the samples. **(d)** Nb/LA vs La/Yb* (Smith *et al.*, 1999) *diagram for source characterisation. **(e)** Ba/Nb vs La/Nb diagram* (Kepezhinskas et al., 2016) *and **(f)** (Hf/Sm)$_N$ vs (Ta/La)$_N$ diagram* (La Flèche et al., 1998) *suggest enrichment by fluid-related subduction metasomatism. SPSL = Superior Province Shoshonitic Lamprophyres, Canada (data from* Wyman *and Kerrich, 1989)*

(Pearce and Peate, 1995), the samples lied in the field of continental arc magmatism (fig 16b), staying above the mantle array, due to subduction enrichment. The Zr/Al_2O_3 vs TiO_2/Al_2O_3 diagram (Müller and Groves, 2000) also plotted the samples in the field of continental/ post-collisional arc setting (fig 16c).

The Nb/La vs La/Yb diagram was also plotted (fig 16d). It suggests that the sampled rocks originate from the lithospheric mantle and have no asthenospheric input. Further, the Ba/Nb vs La/Nb diagram (fig 16e) suggests that these rocks could have formed from subduction-enriched N-MORB-source type rocks.

Finally, the primitive mantle-normalised values plotted on the $(Hf/Sm)_N$ vs $(Ta/La)_N$ diagram (fig 16f) revealed fluid-related subduction metasomatism to be responsible for the geochemical signature of our lamprophyres.

Throughout the diagrams, the samples fell directly into or followed the field of Superior Province Shoshonitic Lamprophyres (SPSL) closely. The SPSL are late Archaean age lamprophyre dykes in the Superior Province of Canada. Wyman and Kerrich (1989) gave the details of SPSL geochemistry and suggested that these lamprophyres are the consequence of magmatism in a subduction-metasomatised mantle.

4.3   Source region and Petrogenetic modelling

By now, it has been established that these lamprophyres are formed by the melting of subduction fluid-metasomatised lithospheric mantle [fig 15(d) and (e)].In the case of SPSL, Wyman and Kerrich (1989) have suggested that a slab-derived LILE-rich aqueous fluid (i.e. high LILE/LREE and LILE/HFSE) metasomatized a MORB-like mantle depleted in Rb as compared to Ba and Sr.

We suspect our source region to consist of depleted mantle enriched by subduction fluid. To quantify the contribution of both the members, mixing calculations were performed following (Langmuir *et al.*, 1978). Elemental ratios of pairs like Ce-Pb, U-Nb, Ba-Sr and Hf-Zr were used to constrain the source since the ratio of these paired elements are unaffected by the processes of partial melting and fractional crystallisation. We found the source to be a mixture of 1 - 4% of average Global

Subducting Sediment (GLOSS) mixed with Depleted Mantle (DM) fig 17a). The plot of Ce/Pb vs Ba/Sr is presented here.
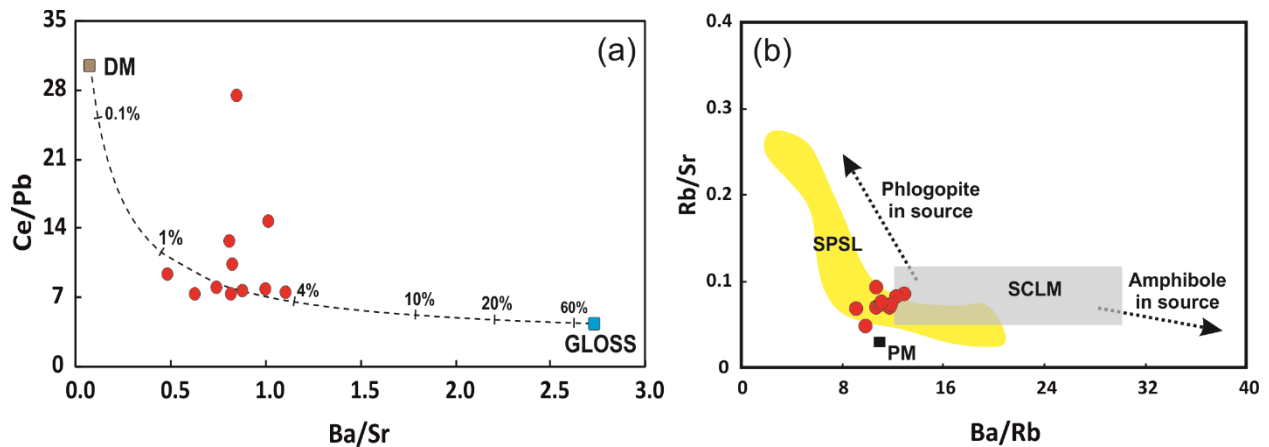

Fig 17 (a) Mixing curve for the mixing of GLOSS and DM (Depleted Mantle) following Langmuir et al. (1978). (b) Rb/Sr vs Ba/Rb diagram (Furman and Graham, 1999) *to determine the presence of amphibole or phlogopite phase in the source region. SPSL = Superior Province Shoshonitic Lamprophyres, Canada (data from* Wyman and Kerrich, 1989*)*

The high fractionation between LREE and HREE in our samples suggests a very low degree of partial melting while the high depletion of HREE indicates the presence of garnet in the source. Rb tends to incorporate in phlogopite more than Sr and likewise Ba partitions into amphiboles more than Rb. Based on this, the Rb/Sr vs Ba/Rb diagram (Furman and Graham, 1999) discriminates between rocks having phlogopite and amphibole in their source. Our samples plotted, as expected, in the field of SPSL and suggest the presence of phlogopite as the hydrous mineral in the source (fig 17b).

Making use of this information, the petrogenesis of the samples was modelled by taking a Phlogopite Garnet Lherzolite source with modal composition as follows: Olivine – 55%, Opx – 19%, Cpx – 7%, Garnet – 11% and Phlogopite – 8%. The source was modelled for non-modal batch partial melting (Shaw, 1970) (melt composition: Olivine – 5%, Opx – 12%, Cpx – 20%, Garnet – 40% and Phlogopite – 23%) followed by crystal fractionation of Olivine (60%) and Cpx (40%) phases. A mixture containing 97% of Depleted Mantle and 3% of GLOSS was considered as the source for calculating source rock elemental concentrations.

The petrogenesis was studied by looking at the Ce/Yb ratio of the samples vs Yb concentration. Ce is an incompatible element and, therefore, it responds well to partial melting and can be used as an index for the degree of partial melting. Yb, on the other hand, being relatively compatible, serves as an indicator of the degree of fractional crystallisation because of its tendency to get incorporated into the crystals. This way, the partial melting curve tends to follow the Ce/Yb axis while crystal fractionation process occurs parallel to the Yb axis.
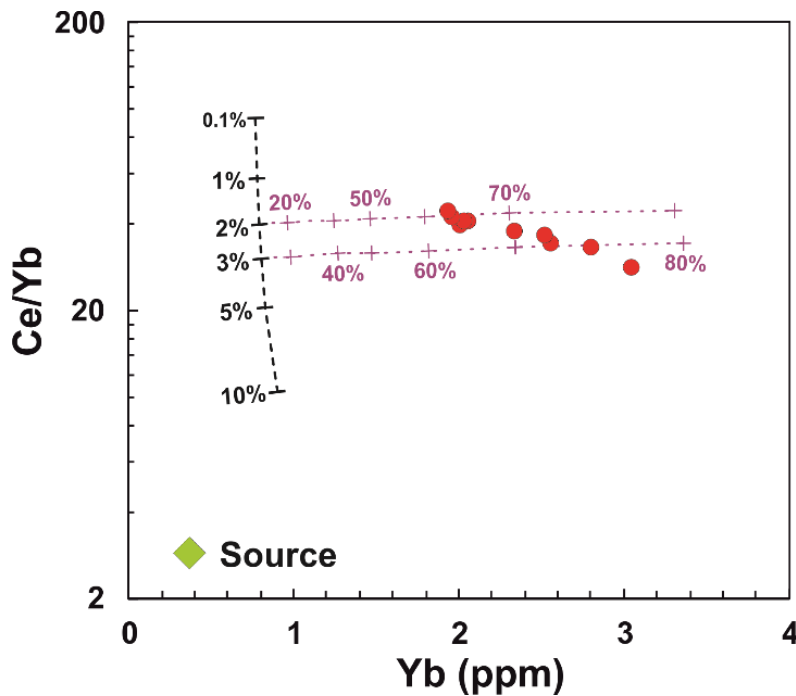

Fig 18 Ce/Yb vs Yb diagram to study the variations brought by different extents of partial melting and fractional crystallisation of the source rock = Phlogopite garnet lherzolite. The black dotted line gives different degrees of partial melting while the magenta lines represent fractional crystallisation.

Plotting the samples on this Ce/Yb vs Yb graph [fig 18] suggests that these lamprophyres likely formed through a low degree (2 – 3%) of partial melting followed by high degrees (60 – 70%) of fractional crystallisation which also explains the low Mg# and Ni content of these lamprophyres. The low degree of partial melting is one of the primary reasons why the magmatism is not voluminous, and these lamprophyres appear as a dyke.

4.4   Geodynamic implication

The U-Pb zircon age of emplacement of the Harohalli dyke swarm has been given as 1192 Ma (Pradhan et al., 2008) which makes the studied lamprophyres Proterozoic. The cratonisation of Dharwar Craton, however, happened between 4000 and 2500 Ma, during Archaean eon. Archean TTGs formed between 4000 and 2600 Ma and remain the major rocks of the Dharwar Craton while sanukitoids and potassic granites formed as intrusions into the TTGs from 3000 to 2500 Ma. (Jayananda et al., 2018)

We have found our lamprophyres to have formed from the partial melting of a depleted mantle which was enriched through fluid-related subduction metasomatism. Therefore, the petrogenesis of these lamprophyres seems to have happened in two stages, as described below.

The first stage involved the Archaean subduction of oceanic crust beneath the Indian continental plate, which constituted the crust building process that is observed throughout the Dharwar Craton. This led to the release of LILE-rich, HFSE and REE-depleted fluid from the subducting slab into the mantle wedge which resulted in a metasomatic enrichment of the (erstwhile depleted) mantle. The craton stabilised over time, keeping the enriched mantle preserved beneath it. The second stage involved a low degree partial melting of the metasomatised mantle in the Proterozoic which, with little crustal contamination, produced these shoshonitic lamprophyres.

Therefore, these lamprophyres extend the previously known subduction-related Archaean tectonics of the Dharwar Craton to the Mysore area of the Western Dharwar Craton.

5   Conclusions

The conclusions of this study are summarised as follows.

a) Petrography of the mafic dykes exposed near Mysore, Western Dharwar craton, concludes that these rocks are lamprophyres. Mineral chemistry classifies them as Vogesites – a type of calc-alkaline lamprophyre – and it is corroborated by the mineralogy.

b) Geochemistry has established these lamprophyres to be shoshonitic in nature and closely following the chemical signature of Superior Province shoshonitic lamprophyres.

c) Presence of Ta-Nb-Ti negative anomaly, Hf-Zr negative anomaly, and absence of clear, dominant crustal contamination has confirmed these rocks to be associated with a subduction setting. Affinity to plume-related magmatism has also been discarded.

d) The petrogenesis of these lamprophyres is through low degree partial melting of a fluid-related subduction-metasomatised depleted mantle. The subduction metasomatism is equivalent to the chemical mixing of average Global Subducting Sediment and Depleted Mantle.

e) Presence of phlogopite and garnet in the source has been inferred from geochemistry. Petrogenetic modelling has shown that Phlogopite garnet lherzolite, upon low degrees of partial melting, followed by high degrees of fractional crystallisation, gives the chemical composition of our samples.

f) The previously proposed subduction regime Archaean tectonics for the Dharwar Craton is associated to the petrogenesis of these lamprophyres which involves an Archaean subduction metasomatism of depleted mantle followed by a Proterozoic magmatism event that produced these shoshonitic lamprophyres.

References

(1)   District Resource Map. The Geological Survey of India, Database-1992.

(2)   Furman, T, Graham, D, (1999) Erosion of lithospheric mantle beneath the East African Rift system: geochemical evidence from the Kivu volcanic province. Lithos 48, 237–262.

(3)   Jayananda, M, Santosh, M, Aadhiseshan, K R (2018) Formation of Archean (3600–2500 Ma) continental crust in the Dharwar Craton, southern India. Earth-Science Reviews. Elsevier, 181, 12–42.

(4)   Kepezhinskas, P K, Eriksen, G M D, Kepezhinskas, N P, (2016) Geochemistry of ultramafic to mafic rocks in the Norwegian Lapland: inferences on mantle sources and implications for diamond exploration. Earth Science Research 5, 148–187.

(5)   Langmuir, C H et al. (1978) A general mixing equation with applications to Icelandic basalts. Earth and Planetary Science Letters, 37, 380–392.

(6)   Leake, B E et al. (1997) Nomenclature of amphiboles. Report of the subcommittee on amphiboles of the International Mineralogical Association Commission on new minerals and mineral names. European Journal of Mineralogy, 9, 623–651.

(7)   Lefebvre, N, Kopylova, M, Kivi, K (2005) Archean calc-alkaline lamprophyres of Wawa, Ontario, Canada: unconventional diamondiferous volcaniclastic rocks. Precambrian Research 138, 57–87.

(8)   La Flèche, M R, Camiré, G, Jenner, G A (1998) Geochemistry of post-Acadian, Carboniferous continental intraplate basalts from the Maritimes Basin, Magdalen Islands, Quebéc, Canada. Chemical Geology 148, 115–136.

(9)   Le Maitre, R W (2002) Igneous Rocks: A Classification and Glossary of Terms (Recommendations of the IUGS Subcommission on the Systematics of Igneous Rocks. Second edition. Cambridge University Press, New York. 236+xvi pp.

(10)   Morimoto, N (1988) Nomenclature of Pyroxenes, Mineralogy and Petrology, 39, 55–76.

(11)   Müller, D, Groves, D I (2000). Potassic Igneous Rocks and Associated Gold–Copper Mineralization. 3rd ed. Springer, Berlin. 252 pp.

(12)   Pearce, J A, Peate, D W (1995) Tectonic implications of the composition of volcanic arc magmas. Annual Review of Earth and Planetary Sciences 23, 251-85.

(13) Peccerillo, A., Taylor, S.R., 1976. Geochemistry of Eocene calc-alkaline volcanic rocks from the Kastamonu area, Northern Turkey. Contributions to Mineralogy and Petrology 58, 63–81.

(14) Pradhan, V R, Pandit, M K, Meert, J G (2008) A cautionary note of the age of the paleomagnetic pole obtained from the Harohalli dyke swarms, Dharwar craton, southern India. In: Srivastava, R K, Chalapathi Rao, N V, Sivaji, C (Eds.), Indian Dykes: Geochemistry, Geophysics, and Geochronology. Narosa Publishing Ltd., New Delhi, India, pp. 339–352.

(15) Rock, N M S (1991) Lamprophyres. Blackie and Sons Ltd., Glasgow. 285 pp.

(16) Shaw, D M (1970) Trace element fractionation during anatexis. Geochimica et Cosmochimica Acta 34, 237–243.

(17) Smith, E I, Sánchez, A, Walker, J D, Wang, K (1999) Geochemistry of mafic magmas in the Hurricane volcanic field, Utah: implications for small- and large- scale chemical variability of the lithospheric mantle. The Journal of Geology 107, 433–448.

(18) Sun, S S, McDonough, W F (1989) Chemical and isotopic systematics of oceanic basalts: implications for mantle composition and processes. In: Saunders, A D, Norry, M J (Eds.), Magmatism in Ocean Basins. Geological Society of London Special Publications Vol. 42, pp. 313–345.

(19) Thorpe, R S (1987) Permian K-rich volcanic rocks of Devon: petrogenesis, tectonic setting and geological significance. Transactions of the Royal Society of Edinburgh 77, 361–366.

(20) Turner, S, Arnaud, N, Liu, J, Rogers, N, Hawkesworth, C, Harris, N, Kelley, S, Van Calsteren, P, Deng, W (1996) Post-collision, shoshonitic volcanism on the Tibetan plateau: implications for convective thinning of the lithosphere and the source of ocean island basalts. Journal of Petrology 37, 45–71.

(21) Wyman, D A, Kerrich, R (1989) Archean lamprophyre dykes of the Superior Province, Canada: distribution, petrology, and geochemical characteristics. Journal of Geophysical Research 94, 4667–4696.